Early Eocene vigorous ocean overturning and its contribution to a warm Southern Ocean

Yurui Zhang[1], Thierry Huck[1], Camille Lique[1], Yannick Donnadieu[2,3], Jean-Baptiste Ladant[4], Marina Rabineau[5], Daniel Aslanian[6]

[1]Univ Brest, CNRS, IRD, Ifremer, Laboratoire d'Océanographie Physique et Spatiale (LOPS), IUEM, Brest, France

[2] Laboratoire des Sciences du Climat et de l'Environnement, LSCE-IPSL, CEA/CNRS/UVSQ, Université Paris-Saclay, Gif-sur-Yvette, France

[3]Aix Marseille Univ, CNRS, IRD, INRA, Coll France, CEREGE, Aix-en-Provence, France

[4] Department of Earth and Environmental Sciences, University of Michigan, Ann Arbor, MI, USA

[5] CNRS, Univ Brest, Univ Bretagne Sud, Laboratoire Géosciences Océan (LGO, UMR6538), IUEM, Plouzané, France

[6] Ifremer, Unité de Recherche Géosciences Marines, Centre de Bretagne, Plouzané, France

Corresponding author: Yurui Zhang (yurui.zhang@univ-brest.fr)

Abstract. The early Eocene (~55 Ma) is the warmest period of the Cenozoic, and is most likely characterized by extremely high atmospheric CO_2 concentrations. Here, we analyze simulations of the early Eocene performed with the IPSL-CM5A2 earth system model, set up with paleogeographic reconstructions of this period from the DeepMIP project and with different levels of atmospheric CO_2. When compared with proxy-based reconstructions, the simulations reasonably capture both the reconstructed amplitude and pattern of early Eocene sea surface temperature. A comparison with simulations of the modern conditions allows us to explore the changes in ocean circulation and the resulting ocean meridional heat transport. At a CO_2 level of 840 ppm, the Early Eocene simulation is characterized by a strong abyssal overturning circulation in the Southern Hemisphere (40 Sv at 60ºS), fed by deep water formation in the three sectors of the Southern Ocean. Deep convection in the Southern Ocean is favored by the closed Drake and Tasmanian passages, which provide western boundaries for the build-up of strong subpolar gyres in the Weddell and Ross seas, in the middle of which convection develops. The strong overturning circulation, associated with subpolar gyres, sustains the poleward advection of saline subtropical water to the convective regions in the Southern Ocean, thereby maintaining deep-water formation. This salt-advection feedback mechanism is akin to that responsible for the present-day North Atlantic overturning circulation. The strong abyssal overturning circulation in the 55 Ma simulations primarily results in an enhanced poleward ocean heat transport by 0.3–0.7 PW in the Southern Hemisphere compared to modern conditions, reaching 1.7 PW southward at 20°S, and contributes to maintaining the Southern Ocean and Antarctica warm in the Eocene. Simulations with different atmospheric CO_2 levels show that the ocean circulation and heat transport are relatively insensitive to CO_2-doubling.

Keywords: Early Eocene, overturning circulation, deep water formation, oceanic heat transport.

1. Introduction

Proxy-based temperature reconstructions suggest that the early Eocene (55–50 Ma) was one of the warmest intervals in the geological history and the warmest of the Cenozoic (Zachos et al., 2001; Cramer et al., 2011; Dunkley Jones et al., 2013). More specifically, the EECO (Early Eocene Climatic Optimum) covers the interval between 53–51 Ma, but shorter (less than tens of thousands of years) hyperthermal events, such as the PETM (Paleocene-Eocene Thermal Maximum) about 55 Ma ago (Zachos et al., 2008), also spanned the early Eocene. The Southern Hemisphere was particularly warm at that time, as shown by inferred surface ocean temperatures exceeding 20°C at high-latitudes (e.g. Evans et al., 2018 and references therein), and by the absence of a perennial ice sheet over Antarctica until the Eocene-Oligocene Boundary (~34) Ma when CO_2 abruptly declined below a certain threshold (Galeotti et al., 2016; Gasson et al., 2014; Ladant et al., 2014). In the early Eocene, high levels of CO_2 in the atmosphere are undoubtedly a critical contributor to the extremely warm climate, with the global temperature increasing by more than 5°C in less than 10 000 years (Zachos et al., 2001, 2008; Huber and Caballero, 2011; Anagnostou et al., 2016), but they do not fully explain the extreme warmth at high-latitudes and the reduced equator-to-pole temperature gradient (Huber and Caballero, 2011).

In addition to this much higher levels of CO_2 in the atmosphere, one of the main differences between the early Eocene and our modern climate lies in the distinct bathymetric and continental configurations, likely resulting in very different ocean circulation (Thomas et al., 2003; Voigt et al., 2013; Winguth et al., 2012; Zachos et al., 2001). In particular, the opening or closing of major oceanic gateways (such as the Drake Passage or the Panama Seaway) during the Late Paleogene and Neogene have been shown to exert a strong influence on the ocean circulation and its associated heat transport (England et al., 2017; Ladant et al., 2018; Nong et al., 2000; Sijp and England, 2004; Toggweiler and Bjornsson, 2000; Yang et al., 2014). Additionally, proxy-based reconstructions and results from Eocene model simulations suggest that the Meridional Overturning Circulation (MOC) was also very distinct from our present day MOC, with no evidence for deep water formation in the North Atlantic until the early Oligocene (Ferreira et al., 2018). Instead, formation of deep water is suggested to happen in the North Pacific (Hutchinson et al., 2018; Winguth et al., 2012) or only in the Southern Ocean (Sijp et al., 2014). Different ocean circulations resulting from different bathymetries are expected to result in different Ocean Heat Transport (OHT). For instance, Sijp and England (2004) found a 0.5 PW decrease in OHT in the Southern Hemisphere in response to the opening of the Drake Passage, but other factors such as CO_2-induced radiative may also contribute to altering OHT (see Huber, 2012 for a review).

In our present-day climate, the ocean is an important actor of the Earth energy balance, as it contributes about one third to the total redistribution of heat from the Equator to the Poles (e.g. Trenberth and Caron, 2001). Although modifications of both the atmosphere and the ocean heat transport (OHT) tend to compensate (Trenberth and Caron, 2001), subtle changes in OHT could trigger large changes in atmospheric extratropical convection, modifying water vapor greenhouse (Rose and Ferreira, 2013) and thereby affecting surface temperatures. The OHT itself results from various contributions, and several attempts have been made in the literature to disentangle the relative roles of the horizontal and overturning ocean circulations in the meridional OHT (Ganachaud and Wunsch, 2003). In the North Atlantic, the strong Atlantic Meridional Overturning Circulation (AMOC) is fed by the formation of dense water by

56 convection at high latitudes, and the AMOC contributes up to 90% of the meridional OHT at 26.5°N (Msadek et al.,
57 2013), where the RAPID monitoring array is located (McCarthy et al., 2015). Based on hosing experiments performed
58 with a climate model (FAOM), Yang et al. (2013) found that the meridional OHT decreases rapidly in response to an
59 artificial shutdown of the AMOC, although Drijfhout and Hazeleger (2006) suggested that on longer (decadal)
60 timescale, the OHT might recover its initial level as the gyre contribution tends to compensate the decrease in OHT
61 associated with the AMOC shutdown. In contrast to the North Atlantic, Volkov et al. (2010) found that, in the Southern
62 Ocean, the OHT results roughly equally from the gyre and overturning contributions.

63 Given the importance of both horizontal and overturning ocean circulations for the meridional OHT, the different
64 MOC and horizontal gyres constrained by the Eocene bathymetry may result in different contributions to the
65 meridional OHT and may potentially contribute to the warm early Eocene climate, in particular in the much warmer
66 high-latitudes. Based on the analysis of early Eocene and present-day simulations performed with the IPSL-CM5A2
67 earth system model, the goal of this study is to better understand what sets the Eocene ocean circulation and the
68 importance of the ocean circulation for the poleward heat transport. The model and simulations used are described in
69 Section 2. In Sections 3 and 4, we examine the MOC and the horizontal circulation, respectively, for the present-day
70 and 55 Ma configurations, and these circulations are then linked to the OHT in Section 5. The sensitivity of the ocean
71 circulation and heat transport to the level of CO_2 in the atmosphere is discussed in section 6. A summary and
72 conclusions are given in Section 7.

73 **2. Numerical model data**

74 **2.1. Model setup and simulations**

75 The simulations used in this study are performed with the IPSL-CM5A2 earth system model (Sepulchre et al., 2019).
76 The oceanic component of IPSL-CM5A2 is NEMOv3.6 (Madec and the NEMO team, 2016), which includes the LIM2
77 sea ice model (Fichefet and Maqueda, 1997) and the PISCES biogeochemical model (Aumont et al., 2015). The
78 atmospheric component is the LMDz model (Hourdin et al., 2013), which is coupled to the land surface model
79 ORCHIDEE (Krinner et al., 2005). Here, we use IPSL-CM5A2 in its standard resolution. NEMO is thus run at a
80 nominal resolution of 2°, increased down to 0.5° at the equator, with 31 levels that vary in thickness with depth. LMDZ
81 is run at a horizontal resolution of 3.75° longitude×1.875° latitude and 39 vertical levels. A full description and
82 evaluation of the IPSL-CM5A2 model can be found in Sepulchre et al. (2019).

83 Two sets of simulations are performed. The first set is composed of the reference preindustrial (PI) simulation (referred
84 to as PI-1x and described in Sepulchre et al., 2019) and another PI simulation in which the atmospheric CO_2
85 concentration is doubled (PI-2x). The second set consists in a baseline simulation of the Early Eocene (hereafter 55
86 Ma-3x), using a setup following the DeepMIP protocol described by Lunt et al. (2017), and two sensitivity experiments
87 to CO_2 (55 Ma-1.5x) and tidal mixing (55 Ma-noM2). In the following, we first briefly describe the baseline Early
88 Eocene simulation (as the DeepMIP guidelines from Lunt et al. (2017) give several options for implementing the Early
89 Eocene boundary conditions), and then precise the boundary condition differences of the two other simulations.

2.1.1. General considerations

Most of the boundary conditions that were adapted for these IPSL-CM5A2 Early Eocene simulations are described in Herold et al. (2014, hereafter H14). Following Lunt et al. (2017), the solar constant and orbital parameters are kept to PI values, so are greenhouse gas concentrations with the exception of atmospheric CO_2. The latter is set to 840 ppm (3x the PI value), so that the simulation is representative of the pre-PETM (following the terminology of Lunt et al., 2017).

2.1.2. Oceanic boundary conditions

The ocean component (NEMO) is commonly run on a tripolar mesh grid (Madec and the NEMO team, 2016), which avoids singularity points in the ocean domain. Because the implementation of the Eocene land-sea mask on the ORCA2 grid would have shifted the singularity points into the ocean domain, we have constructed a new PALEORCA grid, which is designed to run paleo-simulations with IPSL-CM5A2 (see more details in Sepulchre et al., 2019). The bathymetry is obtained by masking out the H14 topography and remapping the resulting bathymetry onto the PALEORCA grid using near-neighbor interpolation. This type of interpolation indeed ensures that small but crucial features of the H14 dataset such as islands and seaways, which may strongly impact the modeled ocean circulation, remain present in the interpolated bathymetry file. Handmade corrections have then been applied at some locations (e.g. in the West African region) to retain oceanic straits that are sufficiently large to allow for exchanges. The Early Eocene bathymetry is shown on Fig. 1.

Modern boundary conditions of NEMO also include forcings of the dissipation associated with internal wave energy from the M2 and K1 tidal components (de Lavergne et al., 2019). The parameterization follows Simmons et al. (2004), with refinements in the modern Indonesian Through Flow (ITF) region according to Koch-Larrouy et al. (2007). To create an Early Eocene tidal dissipation forcing, we directly interpolate the H14 M2 tidal field (obtained from the tidal model simulations of Green and Huber 2013) onto the NEMO grid using bilinear interpolation. In the absence of any estimation of the K1 tidal component for the Early Eocene, we ignore this contribution. In addition, the parameterization of Koch-Larrouy et al. (2007) is not used here because the ITF does not exist in the Early Eocene. The geothermal heating distribution q is created from the 55 Ma global crustal age distribution of Müller et al. (2008), on which the age-heatflow relationship of the Stein and Stein (1992) model is applied:

$$q(t) = 510\, t^{-1/2} \qquad t \leq 55 \text{ Ma}$$

$$q(t) = 48 + 96\, e^{-0.0278\, t} \quad t > 55 \text{ Ma}$$

In regions of subducted seafloor where age information is not available, we prescribe the minimal heatflow value derived from known crustal age. The $1°x1°$ resulting field is then bilinearly interpolated on the NEMO grid. It must be noted that the Stein and Stein parameterization becomes singular for young crustal ages, which yields unrealistically large heatflow values. We thus set an upper limit of 400 mW.m^{-2} on heatflow values, following Emile-Geay and Madec (2009).

Salinity is initialized as globally constant to a value of 34.7 psu following Lunt et al. (2017). The initialization of the model with the proposed DeepMIP temperature distribution (Lunt et al., 2017) led to severe instabilities of the model during the spin-up phase. The initial temperature distribution has thus been modified to follow:

126 $\quad T\ (°C) = \frac{(1000-z)}{1000}\ 25\ cos\ (\varphi) + 10 \quad z \leq 1000$ m

127 $\quad T\ (°C) = 10 \qquad\qquad\qquad z > 1000$ m

128 with φ the latitude and z the depth of the ocean. This new equation gives an initial globally constant temperature of

129 10°C below 1000 m and a zonally symmetric distribution above, reaching surface values of 35°C at the equator and

130 10°C at the poles. This profile gives a 5°C surface temperature reduction compared to the DeepMIP equation (Lunt et

131 al., 2017). No sea ice is prescribed at the beginning of the simulations.

132 The IPSL-CM5A2 model includes PISCES biogeochemical model. Biogeochemical cycles and marine biology are

133 directly forced by dynamical variables of the physical ocean and may affect the ocean physics via their influence on

134 chlorophyll production, which modulates light penetration in the ocean. However, because this feedback does not

135 significantly affect the ocean state significantly (Kageyama et al., 2013) and because the Early Eocene mean ocean

136 color is unknown, we have prescribed a constant chlorophyll value of 0.05 g.Chl/L for the computation of light

137 penetration in the ocean. As a consequence, marine biogeochemical cycles and biology do not alter the dynamics of

138 the ocean and as such, biogeochemical initial forcings have been kept to modern.

139 2.1.3. Continental boundary conditions

140 The atmospheric (LMDZ) and land surface (ORCHIDEE) models run on a low resolution grid but require input

141 forcings at higher resolution. The topographic field is created by masking out ocean points in the H14 reference file

142 and upscaling the 1°x1° masked H14 file to the required LMDZ input topographic resolution (1/6°), as LMDZ includes

143 a subgrid scale orographic drag parameterization requiring high-resolution surface orography (Lott and Miller, 1997;

144 Lott, 1999). A similar procedure is applied to the standard deviation of orography proposed by H14.

145 Following Lunt et al. (2017), the soil properties are prescribed as globally constant to the global mean of the PI

146 simulation. There is no lake module in this version of IPSL-CM5A2. The river routing proposed by H14 is passed to

147 ORCHIDEE at its original resolution of 1°x1°, which ensures an appropriate downscaling to the model resolution.

148 The vegetation cover is prescribed from the BIOME4 reconstruction of H14, using a lookup table (given in Table S2)

149 to convert the 10 megabiomes into ORCHIDEE Plant Functional Types (PFTs). Aerosol distributions are left identical

150 to PI values.

151 2.1.4. Sensitivity experiments and equilibrium

152 We perform two additional Early Eocene experiments. One has the same boundary conditions as the baseline Early

153 Eocene experiment (55 Ma-3x) but an atmospheric CO_2 concentration of 420 ppm (1.5x the PI levels, 55 Ma-1.5x).

154 The other differs from the baseline Early Eocene experiment by the absence of tidal dissipation forcing (55 Ma-3x-

155 noM2).

156 The 55 Ma-3x simulation is initialized from rest and run for 4000 years (Fig. S1). The 55 Ma-1.5x simulation is

157 branched from 55 Ma-3x at year 1500 and run for 4000 years. The 55 Ma-3x-noM2 is branched from 55 Ma-3x at

158 year 3000 and run for 2000 additional years. The two PI simulations are initialized from the Levitus climatology

159 (Boyer et al., 2005), and run for more than 2700 years (Table 1). At the end of all the simulations, the ocean has

160   reached a quasi-equilibrated state and trends in deep ocean temperatures over the final 1000 years of all simulations

161   are smaller than 0.05°C/century.

162   We use the monthly outputs of the last 100 years of each simulation to create a climatological year for each simulation.

163   In the following, we will mostly focus on the comparison between the baseline Early Eocene simulation (55 Ma-3x)

164   and the PI control simulation (PI-1x). The other simulations are analyzed in Section 3 to estimate the contribution of

165   tidal mixing to the oceanic overturning circulation, and in Section 6 to examine the sensitivity of the ocean conditions

166   to different levels of CO_2 in the atmosphere.

167   **2.2. Evaluation of the simulated ocean temperature**

168   This section examines the mean state and the seasonal variation of ocean temperature in the 55 Ma simulations.

169   Further, we evaluate the ability of IPSL-CM5A2 to reasonably simulate the early Eocene sea surface temperature

170   (SST).

171   The annual mean SST in the 55 Ma-3x simulation varies from 10–15°C in the Southern Ocean, to 37.2°C near the

172   Equator (Fig. 2A), with a global mean of 27.5°C. During summer (defined as July-August-September for the Northern

173   Hemisphere and January-February-March for the Southern Hemisphere), the simulated SST reaches ~20°C over most

174   of Southern Ocean (south of 60°S), and up to 38°C in parts of equatorial Indian and Atlantic oceans (Fig. 2A). In the

175   55 Ma-1.5x simulation, both SST and global mean temperature are ~5°C lower than in the 55 Ma-3x simulation (Table

176   1).

177   These simulated SSTs are further compared with proxy-based SST estimates for the early Eocene provided by a recent

178   data compilation performed within the DeepMIP framework (Hollis et al., 2019). The dataset includes 32 records in

179   total, from 4 proxy types (TEX[86], δ^{18}O, Mg/Ca and Clumped Isotope data). The spatial pattern of the simulated SST

180   is overall consistent with the proxy based SST, although significant differences can be observed at some specific proxy

181   data sites (Fig. 2A and S2A).

182   In order to further compare the simulations with the proxy-based reconstructions, we also calculate the root-mean-

183   square deviations (RMSD) between the simulated SST and the reconstructions (Table 2). Although large, the RMSD

184   values are overall of the same order of magnitude as the uncertainties of proxy-based SST estimates, suggesting a

185   reasonable model-data consistency. More importantly, the RMSD values are smaller for the 55 Ma-3x simulation than

186   for the 55 Ma-1.5x simulation, suggesting that the 55 Ma-3x simulation captures better the signal of proxy-based SST

187   reconstructions. This is also consistent with proxy reconstructions suggesting that the atmospheric CO_2 concentrations

188   during the early Eocene were most likely three to four times the PI level (Foster et al., 2017). Additional details on

189   the model-proxy comparison can be found in Supplementary Material.

190   The zonal mean SST in the 55 Ma-3x simulation ranges from 30°C to 37°C in the tropics and decreases toward the

191   high latitudes (Fig. 2B). Within the 40°S–40°N latitudinal band, summer SST remains above 30°C, whereas around

192   60–70°S the annual mean SSTs are ~13°C with a seasonal amplitude of 10 to 15°C. These zonal mean SSTs are overall

193   ~10°C warmer than in the PI-1x simulation, with the largest warmings (as much 12°C) found in the Southern Ocean

194   (Fig. 2B). The warm SSTs found in the Southern Ocean in the 55 Ma simulations also extend at depth (Fig. 2C), with

195 a mean global temperature of 11.3°C in the 55 Ma-3x run, compared to 3.3°C in PI-1x (Table 1). The very warm
196 temperatures found at depth are compatible with several proxy-based temperature estimates (bottom temperatures at
197 1000-5000m between 10 and 15°C, e.g. Huber et al., 2000, their Fig. 4-1). More specifically, Mg/Ca-based
198 temperature estimates suggest that the bottom-water (below 1000 m) temperatures were around 15°C during the early
199 Eocene (Cramer et al. 2011), and Dunkley Jones et al. (2013) found a similar value based on δ^{18}O-Mg/Ca paleo-
200 thermometry for the PETM time-window.

3. The overturning circulation

202 Here we describe the simulated MOC in the different simulations, and investigate the links between the MOC and
203 deep-water formation.

3.1. Meridional overturning circulation

205 The global MOC is represented through the vertical streamfunction ψ computed from the zonally-integrated
206 meridional volume transport as:

$$\psi(z) = \int_W^E \int_{-H}^0 v(x,z)dzdx \qquad (1)$$

208 where v is the meridional velocity, z is the vertical coordinate, H is the ocean depth, x is the zonal coordinate
209 integrated from West (W) to East (E) boundary (meaning that we examine ψ while facing west).

210 In the 55 Ma-3x simulation, a single anticlockwise inter-hemispheric MOC cell fills the whole deep ocean, with a
211 maximum of 40 Sv at 1500 m depth and 60°S (Fig. 3). This strong MOC cell (referred to as SOMOC for Southern
212 Ocean MOC) is associated with the formation of (Eocene) Antarctic Bottom Water (AABW) in the Southern Ocean,
213 flowing northward below about 2000 m. The SOMOC is associated with an upwelling branch extending over the
214 whole Northern Hemisphere, with almost ~26 Sv crossing the equator northward (22 Sv at 20°N and only ~5 Sv at
215 60°N). There is no deep-water formation in the Northern Hemisphere, neither in the North Atlantic nor in the North
216 Pacific.

217 In contrast to the 55 Ma-3x run, the MOC in the PI-1x simulation is composed of the traditional upper and lower cells.
218 The upper cell is clockwise and associated with the AMOC, with a maximum strength of 11–12 Sv reached at 800 m
219 depth around 50–60°N. This cell is fed by the formation of North Atlantic Deep Water (NADW) around 60°N. NADW
220 is transported southward all the way to the Southern Ocean at depth between 1000 and 3000 m, where it is brought
221 back to the surface through wind-induced upwelling, forming the quasi-adiabatic pole-to-pole overturning circulation
222 regime (Marshall and Speer, 2012; Wolfe and Cessi, 2014). The lower cell is anticlockwise, with a maximum strength
223 of 15–16 Sv at 3000 m depth. This anticlockwise circulation is fed by the Antarctic Bottom Water formed by surface
224 buoyancy loss related to ocean-sea-ice interaction (Abernathey et al., 2016), and consumed through mixing process
225 induced by the breaking of internal wave at the sea floor and geothermal heating (Nikurashin and Ferrari, 2013; de
226 Lavergne et al., 2016).

227 The simulated deep-water formation in the Southern Ocean in the 55 Ma simulation is compatible with currently

228 available proxy-based reconstructions of the MOC. Although proxy data constraining the ocean circulation are very

229 limited for the early Eocene, these data seem to point to a common deep-water source around the Austral Ocean during

230 that period (Abbott et al., 2016; Batenburg et al., 2018; Frank, 2002; Thomas et al., 2003, 2014). For instance,

231 Batenburg et al. (2018) reported the convergence of Nd-isotopic signature of sea water across the Atlantic basin from

232 59 Ma onward, and proposed that this convergence is result from an intensification of the intermediate and deep ocean

233 circulation in the Atlantic Ocean, with the dominant deep-water mass originating from the southern high latitudes. In

234 addition, the reconstructed concentration of deep-sea carbonate ion ($[CO_3^{2-}]$) during the Eocene shows a reversed

235 inter-basin gradient compared to the present-day, suggesting a reversed ocean circulation at depth compared to the

236 present-day circulation (Zeebe and Zachos, 2007). Therefore, these proxy data and the simulated ocean circulation are

237 compatible, at least on the direction of the deep circulation and the source of the deep water masses.

238 **3.2. Convection and deep-water formation**

239 The abyssal circulation described in Section 3.1 is fed by deep convection processes that mainly occur in winter. We

240 examine the simulated Mixed Layer Depth (MLD) at the end of the winter season (Fig. 4), which is an efficient

241 indicator of convection. In the 55 Ma-3x simulation, deep convection occurs only at high-latitude in the Southern

242 Hemisphere, with maximum MLD reaching up to 4000 m in the Weddell Sea, and large areas of MLDs deeper than

243 2000 m around Antarctica in the Ross and Amundsen seas (Fig. 4). In contrast, MLDs remain shallow in the Northern

244 Hemisphere, suggesting the absence of any deep convection there. In this hemisphere, the maximum MLDs are found

245 in the North Pacific (350 m) over the poleward western boundary current between 35–50°N, and in the North Atlantic

246 between 35–40°N (300 m), but the deepest MLD at high latitude are only 200 m over the northwest Pacific. Note that

247 the early Eocene North Atlantic basin is limited to a narrow region west of Greenland and poleward of 52°N. In the

248 absence of other sources of deep waters, waters sourced in the Southern Ocean around Antarctica fill the whole abyssal

249 ocean (Fig. 3).

250 In contrast, deep-water formation occurs both in the northern North Atlantic and in the Weddell Sea in the PI-1x

251 simulation (Fig. 4, right column). The deepest MLD (up to 1500 m) are found in the Nordic Seas between 70–75°N

252 and just south of Iceland around 60°N. MLD larger than 1200 m are also found in the eastern Weddell Sea around

253 65°S, indicative of the formation of AABW. This pattern is consistent with the MLD simulated by the CMIP5

254 ensemble for modern conditions (Heuzé et al., 2015).

255 In 55 Ma-3x, the permanent absence of deep convection in the North Pacific is at odds with a few previous model

256 studies and proxy-based reconstruction of the ocean circulation of the early Eocene that have suggested that deep

257 water could form in the North Pacific (Lunt et al., 2010; Abbott et al., 2016). The reasons why deep water forms in

258 the Southern Ocean in the 55 Ma-3x simulation and not in the North Pacific can be linked to the different ocean

259 thermo-dynamical properties of these two regions. Table 3 summarizes key ocean surface variables in the convective

260 regions of the Weddell Sea, where the deepest MLD are found, and of the North Pacific. These two regions roughly

261 correspond to closed Sea Surface Height (SSH) contours around deep convection regions, which are associated with

262   a minimum of SSH— the geostrophic ocean surface currents circulate cyclonically along the SSH contours, so that

263   the interior regions remain largely isolated from surrounding waters. The Weddell Sea is characterized by a strongly

264   reduced vertical stratification compared to the North Pacific, the surface signature of which is much larger surface

265   density (+0.51 kg/m^3). This reduced stratification provides favorable conditions for the emergence of deep convection.

266   According to the equation of state of seawater, the larger surface density found in the Weddell Sea convection region

267   is due to higher salinity (+0.73 psu) contributing to a density increase of 0.57 kg/m^3, partly balanced by warmer

268   temperature (+0.36°C) contributing to a 0.06 kg/m^3 density decrease.

269   Two major causes may explain these large differences in salinity between the two regions: *(i)* the atmospheric

270   circulation and freshwater fluxes to the ocean and *(ii)* the ocean circulation and positive salt-advection feedback. The

271   surface freshwater budget for two extended regions over the Weddell Sea (78°S–61°S and 62°W–8°E) and the North

272   Pacific (48°N–67°N and 124°E–143°W) is shown in Table 3. Averaged precipitation and runoff in the North Pacific

273   box (respectively 1.48 and 0.37 m/yr) exceed those in the Weddell Sea box (1.01 and 0.22 m/yr) by roughly 50%,

274   whereas the evaporation rates are almost similar (0.75 vs 0.71 m/yr). Overall, the average net surface freshwater input

275   is 0.53 m/yr in the Weddell Sea compared to 1.11 m/yr in the North Pacific. Reduced freshwater input by precipitations

276   and continental runoff is related to different atmospheric circulation in the Northern and Southern Hemispheres. In

277   the Southern Ocean, winds largely follow the Antarctic orography (as shown by geopotential height at 850 hPa, Fig.

278   S3), and induce almost no precipitation by orographic uplift over Antarctica coastal regions and no runoff to the

279   Southern Ocean. In contrast, in the North Pacific, the westerlies are blocked by the paleo-Rocky Mountains, especially

280   in the region between 50°N and 70°N. The orographic uplift of moist air masses induces high precipitation (up to 2–

281   3 m/yr) and runoff into the North Pacific (as found in several other models, Carmichael et al., 2016), leading to low

282   sea surface salinity (below 30 psu) along the Pacific coast of North America (not shown) and consequently to increased

283   surface stratification. The upper branch of the MOC and the associated poleward advection of saline subtropical waters

284   constitutes the other contribution to the larger salinities found in the Southern Ocean relative to the North Pacific. This

285   process was sorted out as a positive salt-advection feedback by Ferreira et al. (2018)

286   In contrast, present-day circulation, characterized by deep-water formation in the North Atlantic, is maintained by

287   higher salinities in the North Atlantic than in the North Pacific, which are partly sustained by atmospheric fluxes and

288   the salt-advection feedback (Ferreira et al., 2018). A recent sensitivity study of the impact of topography on modern

289   ocean circulation reveals that the presence of the Rocky Mountains influences the global salinity pattern and the

290   regions where deep convection occurs, through the adjustments of the freshwater transfers between the Pacific and

291   the Atlantic Oceans (Maffre et al., 2018).

292   **3.3. Factors contributing to the vigorous SOMOC**

293   Different factors contribute to the intense SOMOC simulated by the 55 Ma-3x simulation (40 Sv) in comparison with

294   typical present-day MOC, the intensity of which reaches around 18 Sv and 20 Sv for the upper and lower cells

295   respectively (Lumpkin and Speer, 2007). Deep-water formation occurs in the three sectors of the Southern Ocean

296   (Pacific, Atlantic and Indian) but the zonal connections between the different basins hamper a clear quantification of

297 the contribution of each deep-water formation sector to the SOMOC. However, the contributions of the Weddell Sea

298 and the Pacific sector of the Southern Ocean can be estimated because the narrow width of Drake and Tasman passages

299 at 55 Ma (Fig. 1) creates latitudinal continental boundaries on western and eastern sides of these regions. The Weddell

300 Sea, which exhibits the largest MLD in 55 Ma-3x, and the Pacific sector contribute roughly equally to the SOMOC

301 intensity (~ 19 Sv). The South Indian sector contribution is more difficult to assess directly because of the large open-

302 ocean zonal connection with the Atlantic sector.

303 The shallow Drake Passage at 55 Ma provides a western boundary for the development of a subpolar gyre in the

304 Weddell Sea (see Section 4 for more details). This clockwise gyre produces a favorable environment to trigger deep-

305 water formation (known as preconditioning) through isopycnals doming in the center of the gyre, thereby bringing

306 weakly stratified waters of the ocean interior close to the surface (Marshall and Schott, 1999). Clockwise subpolar

307 gyres, and associated deep-water formation by winter convection, are also present in the Pacific sector of the Southern

308 Ocean, in the Ross and Amundsen seas. Previous numerical investigations of the effects of a closed Drake Passage on

309 ocean dynamics have revealed that the closure of the Drake Passage tends to promote the existence of subpolar gyres

310 in the Southern Ocean and vigorous deep-water formation (Nong et al., 2000; Sijp and England, 2004; Ladant et al.,

311 2018). Additionally, it has been recently suggested that the effects of the closure and opening of the Drake Passage

312 and the Panama Seaway may not be independent (Yang et al., 2014; England et al., 2017; Ladant et al., 2018). For

313 instance, Yang et al. (2014) found that closing the Drake Passage tends to suppress the AMOC and to promote the

314 emergence of a strong SOMOC when the Panama gateway is open, whereas the AMOC may remain intense when the

315 Panama gateway is closed. It is thus very likely that, in our 55 Ma simulations, the very shallow Drake Passage,

316 possibly in combination with the opened Panama gateway, contributes to the strong SOMOC.

317 In addition to the influence of the different gateways, tidally-induced mixing, which represents the enhanced vertical

318 diffusivity resulting from the breaking internal waves generated by the interaction of tidal currents with rough bottom

319 topography (St. Laurent et al., 2002), is another factor that contributes to the strong SOMOC found in the 55 Ma-3x

320 simulation. A twin experiment of the 55 Ma-3x simulation, in which no tidal-induced mixing is prescribed (55 Ma-

321 3x-noM2), simulates a SOMOC with a similar structure but an intensity that is 7 Sv weaker (33 Sv, compared to 40

322 Sv in the reference 55 Ma-3x simulation, Fig. S4). It should be noted that the additional simulation has only been run

323 for 2000 years, so that a small part of the difference between the two runs could arise from different equilibrium states.

324 Yet, the difference between these two simulations is consistent with the recent results of Weber and Thomas (2017),

325 who find a 10 Sv MOC enhancement in an early Eocene simulation with the ECHAM5/MPIOM model that explicitly

326 simulates tides compared with a simulation that does not. This suggests that our parameterization for tidally-induced

327 mixing based on the M_2 dissipation fields of Green and Huber (2013) reasonably represents the effect of early Eocene

328 tides on global ocean circulation. The strengthening of the MOC induced by tidal mixing can be directly related to the

329 driving role of diapycnal mixing on the overturning circulation. Numerous studies have demonstrated that both the

330 magnitude and the vertical distribution of the diapycnal mixing largely affects the strength of the MOC (Bryan, 1987;

331 Manabe and Stouffer, 1999). As already pointed out by Green and Huber (2013), the Eocene MOC may be much more

332 sensitive to the intensity of the abyssal mixing than the present day AMOC, that is largely isolated from the ocean

floor by the presence of AABW and sustained quasi-adiabatically by the wind-driven upwelling in the Antarctic Circumpolar Current (ACC; Marshall and Speer, 2012). Diapycnal mixing is the only process that can warm up the dense waters formed in the Eocene Southern Ocean, and these dense waters are directly exposed to the tidally-induced mixing at the bottom, such that the abyssal dissipation becomes the main controlling factor of the SOMOC intensity. In this respect, the large tidal dissipation rate suggested by Green and Huber (2013) in the Pacific is particularly important.

Another often-mentioned factor affecting ocean circulation is the climate state, in response to the atmospheric CO_2. Based on highly simplified models, theoretical studies have suggested that ocean ventilation tends to increase under a warmer climate state due to a higher sensitivity of seawater density to temperature (e.g. de Boer et al., 2007). However, the deep-water formation is a very regional phenomenon and, thus, this idealized relationship might be complicated by other regional-scale factors. Indeed, we do not see any systematic change in SOMOC between two simulations with different CO_2 levels (1.5x and 3x) (see Section 6 for further discussion).

4. Horizontal circulation and winds

In the present day North Atlantic, vertical and horizontal circulations are intimately connected, especially in the subpolar gyre (Marshall and Schott, 1999). For instance, the warm North Atlantic Current flowing northward and the cold East Greenland Current flowing southward are found roughly at the same depth at 60°N, such that the MOC in z-coordinates does not capture the associated water mass transformation at high latitude, whereas the MOC in density coordinates does (Zhang, 2010). It is only when the cold branch deepens in the Labrador Sea and becomes the Deep Western Boundary Current off Cape Hatteras that the overturning streamrerefunction in z-coordinates provides a good estimate of the water mass transformation. From this perspective, the horizontal subpolar gyre is integral part of the North Atlantic thermohaline circulation. By analogy, a similar intricacy between horizontal gyres and the thermohaline circulation can be expected to exist in the early Eocene Southern Ocean, where the near-closure of the Drake and Tasmanian passages allows for the emergence of intense subpolar gyres, which can precondition and feed the formation of deep water sustaining a strong SOMOC. We thus examine in the following the horizontal ocean circulation during the Eocene.

4.1. Gyre circulations

In the 55 Ma-3x run, several horizontal gyres are well developed in both hemispheres, as shown by the barotropic streamfunction (Fig. 5). In particular, the quasi-closed Drake and Tasmanian passages support the western boundary currents necessary for the buildup of intense subpolar gyres in each sector of the Southern Ocean. The intensity of each gyre is respectively 40 Sv in the Weddell Sea, 35 Sv in the Indian sector, and 28 Sv in the Ross and Amundsen Seas in the Pacific sector, and winter convection and deep water formation occurrs in the center of these gyres, as it is the case in the modern Labrador Sea (Marshall and Schott, 1999). The formation of deep water in the subpolar gyres is also promoted by the advection of saline subtropical waters from the subtropical gyres southward flowing branch (visible for instance on sea surface salinity), as shown by Ferreira et al. (2018). Compared to the PI conditions, the

subtropical gyres are strongly perturbed by the numerous open gateways connecting the different basins. In the Southern Hemisphere, due to the large opening between Australia and Asia, the main subtropical gyre extends over both the paleo-Indian and Pacific oceans, with a western boundary current leaning partly on the northern coast of Australia (up to 52 Sv), Madagascar (60 Sv) and Africa. This 'super'-subtropical gyre is partly fed by a 31 Sv eastward flow south of the Cape of Good Hope originating from the South Atlantic subtropical gyre. Fig. 5 also reveals the existence of a strong anti-clockwise subtropical gyre south of a clockwise subpolar gyre in the North Pacific, with maximum intensity of ~42 and 13 Sv respectively. In contrast, the gyres in the tectonically-restricted North Atlantic basin (Fig. 1) are weak, with maximum intensity of 22 Sv and 2 Sv for the subtropical and subpolar cells respectively. The numerous gateways in the tropical band clearly complicate the traditional gyre pattern in each basin, and increase global connectivity between ocean basins.

In the PI-1x simulation, the maximum intensity of the North Atlantic subtropical and subpolar gyres are respectively 37 and 19 Sv, which is comparable with the intensity of the gyres found in the Southern Hemisphere in the 55 Ma simulations. The most salient feature of the PI-1x simulation is the existence of the Antarctic Circumpolar Current (ACC), with an eastward transport of 108 Sv through the Drake Passage, which totally disrupts the subtropical-subpolar gyres circulation in the different basins of the Southern Hemisphere. In many respects, the South Atlantic and the Weddell Sea during the Eocene are thus an analogue of the present-day North Atlantic in terms of intertwining of subtropical, subpolar and overturning circulation.

4.2. Wind stress

Modern ocean circulation, in particular in the surface layers, is largely driven by the surface winds (e.g. Munk, 1950), and it is thus interesting to examine the difference between the PI and 55 Ma horizontal circulation in light of changes in the wind pattern.

Overall, the patterns of the wind stress at the ocean surface in the 55 Ma-3x and PI-1x simulations are similar (Fig. 6), although the magnitude differs between the simulations. The sign of this wind stress difference depends on the hemisphere considered. For instance, wind stress is about 30% weaker in 55 Ma-3x than in PI-1x in the Southern Hemisphere (by 0.05 N m^{-2} at 45°S) whereas it is slightly stronger in the Northern Hemisphere. In the Southern Hemisphere, the difference is particularly striking in the South Atlantic and Indian basins and is largely due to the blocking position of Australia in the early Eocene. The paleogeographic context also explains the increased symmetry in zonal wind stress fields between the Eocene hemispheres relative to the PI.

The more symmetrical pattern of wind stress at the ocean surface in the 55 Ma-3x simulation (compared to PI-1x) is also observed in the zonal wind fields from the surface to 500 hPa in the atmosphere (Fig. 6D). The zonal wind strength is largely determined by the meridional temperature gradient in the atmosphere through the thermal wind relation (Holton and Staley, 1973). Indeed, the meridional temperature gradient in the 55 Ma-3x run (compared to PI-1x) is much reduced in the Southern Hemisphere south of 40°S in a large part of the air column, (roughly from the surface to at least 500 hPa) in good agreement with the weaker westerly winds found in the 55 Ma-3x run (Fig. 6D). Moreover,

401   the positions of Australia, Africa, and South America are located much more southward during the Eocene than the

402   present-day, result in a blocking effect on zonal winds, reducing the wind stress at 500 hPa by a maximum of 18% at

403   40°S. In the Northern Hemisphere, the meridional temperature gradient in the 55 Ma-3x simulation is reduced at the

404   surface only north of 60°N and similar at 500 hPa relative to the PI-1x, whereas the zonal winds are slightly stronger

405   in 55 Ma-3x simulation throughout the air column compared to the PI-1x. At the surface, the maximum zonal wind

406   stress is 19% stronger and shifts poleward by 2°, mainly due to land-sea distribution.

407   Changes in ocean gyre circulation between the 55 Ma and PI configurations are mostly due to the large changes in the

408   ocean basin geometry and gateways rather to the moderate changes in the strength and patterns of the wind stress (and

409   its curl). A full understanding of what sets the gyres intensity in the 55 Ma simulations (as well as in the PI simulations)

410   would require further investigations, which are beyond the scope of the present paper.

411   **5. Oceanic heat transport and its decomposition**

412   Modern ocean circulation plays a key role in the regulation of climate through its contribution to the redistribution of

413   heat from the Equator to the Poles. In the tropics, the ocean transports roughly 50% of the 3 PW carried northward by

414   the ocean–atmosphere system, but less than 10% of the total at high latitude (Trenberth and Caron, 2001). The relative

415   contributions of the horizontal and overturning ocean circulations to the meridional heat transport also vary greatly

416   over different latitudes and between oceanic basins (Ganachaud and Wunsch, 2003). In light of the different ocean

417   circulations found in the Eocene and PI conditions, we further investigate in the following how efficient the ocean

418   was at transporting heat across latitudes in the early Eocene.

419   **5.1. Oceanic heat transport**

420   The total meridional OHT at a given latitude y is defined as the sum of advective and diffusive contributions:

421

$$OHT_{total} = \rho_0 C_p \int_W^E \int_{-H}^0 \left(v\theta + K_H \frac{d\theta}{dy} \right) dzdx \qquad (2)$$

422   where ρ_0 is the seawater density, C_p is the specific heat capacity of sea water, v is the meridional velocity, θ is the

423   potential temperature, K_H is the horizontal diffusivity coefficient, and H is the ocean depth. Here the computation is

424   performed from the model outputs at each model time step. In the early Eocene simulations, there is a significant

425   increase in OHT in the Southern Hemisphere compared to the present-day simulations, but a decrease in the Northern

426   Hemisphere (Fig. 7). As a result, the simulated OHT in the 55 Ma-3x experiment is remarkably asymmetric between

427   hemispheres. The mean OHT difference between the 55 Ma-3x and PI-1x simulations is of the order of 0.2 PW (1 PW

428     $= 10^{15}$ Watt), peaking at 0.5 PW around 35°S. The 55 Ma-3x OHT reaches a maximum of 1.7 PW at 15–20°S, that is

429   ~0.3 PW larger than in the present-day simulations at the same latitude but also ~0.5 PW larger than the maximum PI

430   value of the Northern Hemisphere. This enhanced OHT in the Southern Hemisphere contributes to maintaining the

431   Southern Hemisphere particularly warm in the early Eocene, especially south of 50°S, as can be seen on the SST

432   distribution (Fig. 2).

13

Previous studies have examined the role of OHT during the Eocene with a particular focus on the response of the OHT to the opening of Southern Ocean gateways in either realistic Eocene paleogeography or more idealized modern configurations. The OHT simulated by our 55 Ma-3x experiment lies within the range of values found in the literature. For instance, using the NCAR CCSM ocean model with surface heat flux boundary conditions mimicking an energy-balanced atmospheric model, Nong et al. (2000) found that closing the Drake Passage in a modern configuration results in a stronger SOMOC (24 vs 12 Sv), associated with an increased poleward OHT in the Southern Hemisphere (+0.2 PW, from 1 to 1.2 PW) and a decreased OHT in the Northern Hemisphere. Similarly, using the UVic intermediate complexity Earth System Climate Model, Sijp and England (2004) found a strongly enhanced heat transport (from 1.6 to 2.4 PW) in the Southern Hemisphere in response to the closure of Drake Passage in a modern configuration. Using the fully coupled NCAR model with a realistic Eocene configuration in which the Drake Passage has a similar configuration to the one we use but the closed Tasmanian gateway is closed, Huber et al. (2004) performed a set of simulations that exhibited rather weak poleward OHT in the Southern Hemisphere (with a maximum of 0.9 PW at ~10ºS), likely because of the absence of a strong SOMOC in their simulations. When closing the Drake passage in an otherwise modern configuration with the GFDL model, Yang et al. (2014) found that the change in OHT was much larger when the Panama Seaway was open, with a strong increase of the OHT in the Southern Hemisphere. More recently, Baatsen et al. (2018) used the higher resolution CESM earth system model to simulate the later Eocene (38 Ma) climate, with levels of CO_2 and CH_4 in the atmosphere prescribed to 2 and 4 times the PI levels. In these two simulations, Baatsen et al. (2018) found a maximum of ~1.5 PW OHT at 20ºS in the Southern Hemisphere, associated with a 14–16 Sv SOMOC (compared to the 40 Sv and 1.7 PW at the same latitudes in our 55 Ma-3x simulation).

Although these previous studies are all based a variety of models with different complexity and resolution, the results consistently suggest that the OHT is largely coupled to the structure and strength of the MOC cells. For instance, the difference in MOC intensity simulated by coupled and uncoupled models could be primarily caused by the positive salt-advection feedback and the self-stabilizing thermal feedback (Sijp and England, 2004). It is noteworthy that the strengthening influence of tidal-induced mixing on the MOC (+7 Sv) is associated with a rather weak increase in OHT, lower than 0.03 PW on average, in agreement with Weber and Thomas (2017). Such a nonlinear relationship between OHT and MOC has also been suggested by Boccaletti (2005), who argued that the shallow circulation `locally` can be as important as the deep overturning for determining the OHT.

5.2. Decomposition of the meridional ocean heat transport

In order to understand the differences in OHT among our simulations (Fig. 7A), we further split up the OHT into an advective contribution (OHT_{adv}) and a diffusive contribution, corresponding respectively to the first and second term on the RHS of Eq. 2 (Fig. 7B and 7C). This decomposition reveals that, in both the 55 Ma-3x and the PI-1x simulations, the advective part dominates the OHT at all latitudes, except at 40°S/N in PI-1x where the presence of large temperature gradient (Fig. 2B) results in larger diffusive heat transports. Figs. 7B and 7C also reveal that different OHT between PI-1x and 55 Ma-3x are mainly due to differences in the advective components, and the differences in diffusive OHT being rather small.

469　The advective component, OHT_{adv}, can be decomposed further into an overturning (OHT_{MOC}) and a gyre (OHT_{gyre})
470　component, following for instance Bryan (1982) or Volkov et al. (2010):

$$OHT_{adv} = \rho_0 C_p \underbrace{\iint \bar{v}\bar{\theta} \, dx \, dz}_{OHT_{MOC}} + \rho_0 C_p \underbrace{\iint v'\theta' \, dx \, dz}_{OHT_{gyre}} \qquad (3)$$

472　where $\bar{v}$, $\bar{\theta}$ represent the zonal averages of the velocity and temperature, respectively, and v', and θ' the deviations
473　from these zonal means. The first term of the RHS of Eq. 3 corresponds to the overturning component (OHT_{MOC}) and
474　the second term corresponds to the horizontal transport associated with the large-scale gyre circulation (OHT_{gyre}).
475　Note that due to limitations on the availability of model outputs, the different terms of Eq. 3 presented on Figs. 7D
476　and 7E are computed from monthly means. This explains why the sum of the two terms does not completely equal
477　OHT_{adv} shown on Fig. 7C, since the latter is computed at each model time step during the simulations. The differences
478　between the two computations can be seen on Fig. 7C.

479　The decomposition reveals that the enhanced Southern Hemisphere OHT_{adv} in 55 Ma-3x (compared to PI) is overall
480　due to differences in OHT_{MOC} (Fig. 7D, 7E). The contribution from gyre circulation varies with latitude, with a
481　compensation effect between OHT_{gyre} and OHT_{MOC} in the low-latitudes and an enhancement in mid-to-high latitudes.
482　Consequently, the overall larger OHT_{adv} in the tropics of 55 Ma-3x simulation is primarily contributed from the strong
483　Eocene OHT_{MOC} (up to 2 PW), which is ~0.3 PW larger than in the PI simulations. In the mid-latitudes of the Southern
484　Hemisphere, where the OHT_{adv} is overall smaller than in the tropics, the OHT_{MOC} in 55 Ma-3x is almost 1 PW stronger
485　than in PI-1x. By contrast, south of 60°S, enhanced OHT_{adv} in 55 Ma-3x (compared to PI) results from the combination
486　of stronger OHT_{gyre} and OHT_{MOC}. It is worth noticing that OHT_{gyre} at ~40°S in the PI-1x simulation is very likely
487　underestimated in our decomposition computed from monthly mean data, because higher-frequency processes
488　(resulting for instance from atmospheric synoptic variability) could contribute significantly to OHT_{gyre} in regions
489　where the mean meridional currents are weak (Volkov et al., 2010).

490　It is obvious from Figs. 3 and 7 that the vigorous SOMOC simulated in the 55 Ma-3x experiment drives a strong net
491　OHT toward the South Pole. This strong SOMOC is associated with poleward transport of warm waters at shallow
492　depths where zonal oceanic temperature gradients are larger and with a returning equatorward transport of colder
493　water at depth where ocean temperature tends to be more homogenous (Fig. 2C). Remarkably, although the ACC is
494　absent from the Eocene simulation because of different configurations of the Drake and Tasmanian passages that
495　constitute latitudinal barriers (Munday et al., 2015), the contribution of the gyre circulation and diffusive process to
496　poleward heat transport (OHT_{gyre}) is smaller than in the preindustrial simulations. This small OHT_{gyre} in the Eocene
497　Ma simulation is unexpected, given previous hypotheses on the climatic effects of the ACC (e.g. Nong et al., 2000;
498　Toggweiler and Bjornsson, 2000; Sijp and England, 2004). The ACC has indeed been suggested to be a barrier for
499　poleward heat transport, so that the onset of the ACC could be a potential driver for the Antarctica cooling Eocene-
500　Oligocene Transition around 34 Ma. However, these studies may not have captured the full complexity of the links
501　between the ACC and OHT in the Southern Ocean. The analysis of both in-situ observations (Watts et al., 2016) and

502 the CESM1.0 model (Yang et al., 2015) have indeed revealed that the ACC is composed of meridional excursions of

503 the mean geostrophic horizontal shear flow, energetic eddies and large diffusive heat transport, which balances out

504 equatorward OHT due to Ekman transport and leads to a net poleward OHT in the Southern Ocean (Volkov et al.,

505 2010).

6. Sensitivity of the ocean response to a doubling of the levels of atmospheric CO_2

507 Our analysis has so far focused on the comparison between the 55 Ma-3x and PI-1x simulations, as the former is

508 performed with atmospheric CO_2 levels considered to be representative of the early Eocene (Foster et al., 2017; Lunt

509 et al., 2017). The analysis of two additional simulations (55 Ma-1.5x and PI-2x) allows us to investigate the robustness

510 of the ocean circulation in this range of atmospheric CO_2 concentrations. These simulations also help us to quantify

511 the sensitivity of the oceanic conditions to a doubling of the CO_2 levels in the atmosphere under the early Eocene and

512 modern setting.

513 The mean ocean temperatures are very sensitive to the atmospheric CO_2 concentration in the Eocene configuration

514 (Table 1). The global mean ocean temperature in the Eocene simulations increases by 4.9ºC in response to CO_2

515 doubling from 1.5x to 3x, which is much larger than the 1ºC increase in PI simulations from 1x to 2x. The global mean

516 SST in the Eocene also shows a much larger increase as response to a CO2 doubling (+4.7°C) than in the preindustrial

517 (+2.6°C), especially at high latitudes and in the regions of deep-convection of the Southern Ocean (Fig. 8), which is

518 similar to the changes in air temperature at 2 m (+5.6°C vs +3.5°C respectively, this difference is known as the climate

519 sensitivity). Such contrasted values of climate sensitivity between 55 Ma and PI are in good agreement with the recent

520 results of Farnsworth et al. (2019) obtained with the HadCM3BL model. In the absence of perennial sea-ice in 55 Ma

521 simulations, the winter SST in deep-convection regions is largely influenced by the air-sea interactions and thus

522 directly related to air temperature, which rarely decreases below 10°C (resp. 5°C) in 55 Ma-3x (resp. 1.5x), such that

523 the deep waters filling the whole ocean interior vary accordingly with temperature. This is not the case in the present-

524 day configuration where deep-water formation is tied to marginal ice zones, such that dense waters formed by brine

525 rejection have initial temperatures close to freezing. Intuitively, we could have expected a larger sensitivity of ocean

526 temperature to atmospheric CO_2 in the PI runs because of the ice-albedo feedback. Yet, the effect of this feedback

527 appears to be limited to the high latitudes (Fig. 8) and only plays a marginal role in the changes in global mean SST

528 or temperatures of the deep water masses (Table 1).

529 The ocean circulation exhibits only a minor response to a CO_2 doubling in both the Eocene and preindustrial

530 configurations, although this response locally varies (Table 4). In the 55 Ma simulations, the doubling of CO_2 level

531 marginally enhances the maximum abyssal SOMOC (by 0.3 Sv out of 40 Sv in total), while the intensity of the shallow

532 MOC cell and of the barotropic streamfunction are slightly reduced. In the PI simulations, the doubling of atmospheric

533 CO_2 levels has the opposite effect on the AABW, whose maximum intensity reduces by 1.2 Sv (out of ~15 Sv), whilst

534 the AMOC slightly increases by 0.3 Sv (out of ~11 Sv). This small increase in the steady-state AMOC is quite

535 interesting and needs to be contrasted with the transient response of the AMOC intensity to global warming (Gent,

16

2018; Jansen et al., 2018). Indeed, CMIP-type climate models consistently project strong decline of the AMOC strength when forced with a range of increasing greenhouse gas emission scenarios (Schmittner et al., 2005; Cheng et al., 2013). Yet, when run for longer integrations until full equilibrium, models suggest that the AMOC tends to recover and that the AMOC is ultimately not very sensitive to the CO_2 levels (Jansen et al., 2018; Thomas and Fedorov, 2019), as is the case in our PI simulations. Once equilibrium is reached, the most significant effect of a CO_2 doubling in our PI experiments is a sharp increase in the ACC transport (+22 Sv out of 108 Sv in PI-1x), in response to stronger westerlies in the Southern Ocean. In contrast, the barotropic circulation remains almost the same in the Pacific, but varies in the North Atlantic with a 5 Sv stronger (weaker) subpolar (subtropical) gyre in the PI-2x simulation compared to PI-1x.

A number of paleoclimate studies have investigated the influence of CO_2 levels on ocean circulation in coupled models, with contrasted responses depending on the period considered and the model used. For instance, the deep overturning circulation in the HadCM3L climate model shows an overall high sensitivity to CO_2 concentrations in the PETM simulations (Lunt et al., 2010), whilst the GENIE model only exhibits a small response in the Cretaceous simulations of Monteiro et al. (2012). Winguth et al. (2010) further suggest that, in a given simulation of the Paleocene-Eocene period, the different MOC cells (e.g. in the Northern and Southern hemispheres) could respond differently to a change of CO_2 levels. These various responses can be attributed to different factors. First, it is clear that the resolution and overall complexity of the model may partly control the sensitivity of the MOC to CO_2 levels, as in models of modern climate (e.g. Bryan et al., 2006). Second, a variety of time scales are intertwined in the adjustment of ocean circulation to external perturbations, from decades for the dynamical adjustment to millennia for the thermo-dynamical response of bottom waters through vertical advective-diffusive balance (e.g. Donnadieu et al., 2016). The transient response of the ocean can therefore differ, or even be in the opposite direction, from the final equilibrium response.

The OHT response to a doubling of CO_2 in the Eocene simulations is also small, with a slight decrease, in contrast to the OHT increase seen in the PI simulations (although the magnitude of the change is smaller; Fig. 9A). The OHT in the 55 Ma-3x simulation is about 0.15 PW smaller than in 55 Ma-1.5x simulation over most latitudes. Both overturning and horizontal components contribute to this overall smaller OHT in the 55 Ma-3x simulation (Fig. 9D, 9E). A weak OHT in the tropics is due to weaker MOC at the same latitudes, while a weak OHT at high latitudes can be attributed to the smaller amplitude of horizontal gyres. In the PI simulations, the OHT in the PI-2x simulation is ~0.1 PW larger than in PI-1x at high latitudes. This larger OHT in PI-2x is mostly due to the gyre component, which is in good agreement with the ~5 Sv stronger North Atlantic subpolar gyre and almost no change in the AMOC for instance.

Our results therefore support a stable, yet rather small, response of global ocean circulation and heat transport to the doubling of atmospheric CO_2 levels. Nevertheless, we have only investigated a limited range of CO_2 levels (from 1.5x to 3x) and cannot exclude that the sensitivity of ocean circulation to CO_2 concentrations may change at more extreme CO_2 levels, as this sensitivity may be highly non-linear (Lunt et al., 2010). Given that the early Eocene atmosphere CO_2 levels are relatively poorly constrained by proxy reconstructions, additional experiments are underway to explore the model response to higher CO_2 concentrations in the early Eocene configuration.

7. Conclusions

Numerous proxy based reconstructions have revealed that the early Eocene (~55 Ma) was most likely the warmest period in the Cenozoic. During that period, paleogeographic restrictions of certain modern basins and gateways, such as the North Atlantic and the Drake and Tasmanian passages, suggest fundamental differences with the modern large-scale ocean circulation. It has been proposed that the distinct mode of ocean circulation operating during the early Eocene may have contributed to the significant polar warmth recorded by observational evidence. There is however no consensus on the modes of early Eocene ocean circulation or on the relative influence of the overturning and horizontal circulation on the poleward heat transport. Here we revisit this question by analyzing the ocean circulation and its contribution to the meridional OHT using simulations of the early Eocene performed with the IPSL-CM5A2 earth system model set up with the recent paleogeographic reconstruction of this Eocene time slice distributed as part of the DeepMIP project. Our main results are summarized hereafter.

A strong abyssal overturning circulation (up to 40Sv) is found in the 55 Ma simulation, with deep water formed only in the Southern Ocean (mainly in the Weddell Sea), whereas there is no deep water formation in the Northern Hemisphere, in contrast to some previous work on the early Eocene (e.g. Winguth et al., 2012). This situation is favored by orographically-induced freshwater fluxes (precipitation and runoff) and maintained by a salt-advection feedback. Indeed, the atmospheric circulation around Antarctica induces relatively low precipitation rates in the Southern Ocean, resulting in higher salinity, and hence larger surface density than in the North Pacific, where the orographic precipitations and runoff induced by the presence of the paleo-Rockies tend to reduce surface salinity and inhibit deep water formation.

The paleogeography (and paleobathymetry) and tidally-induced mixing are the main drivers of the strong SOMOC during the early Eocene. The (nearly-)closed Drake and Tasmanian passages are of fundamental importance for sustaining the SOMOC, via their effect on horizontal ocean circulation. More specifically, with the (nearly-)closed Drake and Tasmanian Passages serving as a western boundary, clockwise subpolar gyres are well-developed (~40 Sv) in the Weddell and Ross Seas, thereby favoring the emergence of deep convection and deep-water formation through isopycnal doming and salt-advection feedback. Tidal-induced mixing also contributes to 7 Sv (out of 40 Sv) to this SOMOC, but with only a limited impact on the heat transport.

The vigorous SOMOC simulated for the Eocene is associated with a larger poleward OHT (by a maximum of 0.5 PW relative to PI) in the Southern Hemisphere that largely contributes to maintaining a warm Southern Ocean and Antarctica. Perturbation experiments have been conducted in present-day coupled models to evaluate the impact of an AMOC shutdown. In their model, Vellinga and Wood (2008) found that a 10 Sv reduction in AMOC, associated with a change of its structure, leads to a 1.7°C cooling of the Northern Hemisphere, with a local stronger cooling by 5°C in the northern North Atlantic. This gives credit to the importance of the 40 Sv SOMOC for maintaining the Southern Ocean warm in the 55 Ma simulations. However, other factors than a strong SOMOC and associated OHT could contribute to the warm Southern Ocean. Rose and Ferreira (2013) have shown that changes in OHT can induce changes in global mean temperature and meridional temperature gradient through convective adjustment of the extratropical

606 troposphere and increased greenhouse effect. According to their results, the magnitude of those changes could be up
607 to 1°C and 2.6°C for every 0.5 PW enhancement in OHT. Further investigations would be required to examine if this
608 mechanism is also at play in our simulation and whether it contributes significantly to Southern Ocean warmth.

609 A further decomposition of the OHT reveals that the different overturning circulations between the early Eocene and
610 the preindustrial explain most of the increase of the OHT in the Southern Hemisphere. The contribution of gyre
611 circulation to the OHT is only secondary, and varies with latitude, with a compensating effect between the MOC and
612 gyre circulations in the low- and mid-latitudes, whereas the two contributions add up in the high latitudes. More
613 importantly, the latitudinal distribution of the gyre contribution to the OHT only marginally varies between the early
614 Eocene and preindustrial simulations, despite the absence of the ACC in the early Eocene experiment. Given that the
615 55 Ma paleo-bathymetry does not allow the existence of a strong ACC, this result questions strongly the idea that the
616 ACC could be a strong barrier for OHT in our modern climate, and suggests that the meridional excursions of the
617 ACC might indeed play an important role in the gyre-related OHT (Volkov et al., 2010; Watts et al., 2016; Yang et
618 al., 2015).

633 **References**

634 Abbott, A. N., Haley, B. A., Tripati, A. K. and Frank, M.: Constraints on ocean circulation at the Paleocene–Eocene
635 Thermal Maximum from neodymium isotopes, Clim Past, 12(4), 837–847, doi:10.5194/cp-12-837-2016, 2016.

636 Abernathey, R. P., Cerovecki, I., Holland, P. R., Newsom, E., Mazloff, M. and Talley, L. D.: Water-mass
637 transformation by sea ice in the upper branch of the Southern Ocean overturning, Nat Geosci, 9, 596,
638 doi:10.1038/NGEO2749, 2016.

639 Anagnostou, E., John, E. H., Edgar, K. M., Foster, G. L., Ridgwell, A., Inglis, G. N., Pancost, R. D., Lunt, D. J. and
640 Pearson, P. N.: Changing atmospheric CO_2 concentration was the primary driver of early Cenozoic climate, Nature,
641 533, 380, 2016.

642 Aumont, O., Ethé, C., Tagliabue, A., Bopp, L., and Gehlen, M.: PISCES-v2: an ocean biogeochemical model for
643 carbon and ecosystem studies, Geosci. Model Dev., 8, 2465–2513, https://doi.org/10.5194/gmd-8-2465-2015, 2015.

644 Baatsen, M., von der Heydt, A. S., Huber, M., Kliphuis, M. A., Bijl, P. K., Sluijs, A. and Dijkstra, H. A.:
645 Equilibrium state and sensitivity of the simulated middle-to-late Eocene climate, Climate of the Past Discussions, 1–
646 49, doi:10.5194/cp-2018-43, 2018.

647 Batenburg, S. J., Voigt, S., Friedrich, O., Osborne, A. H., Bornemann, A., Klein, T., Pérez-Díaz, L. and Frank, M.:
648 Major intensification of Atlantic overturning circulation at the onset of Paleogene greenhouse warmth, Nat
649 Commun, 9(1), 4954, doi:10.1038/s41467-018-07457-7, 2018.

650 Boccaletti, G.: The vertical structure of ocean heat transport, Geophys Res Lett, 32(10), L10603,
651 doi:10.1029/2005GL022474, 2005.

652 de Boer, A. M., Sigman, D. M., Toggweiler, J. R. and Russell, J. L.: Effect of global ocean temperature change on
653 deep ocean ventilation, Paleoceanography, 22(2), PA2210, doi:10.1029/2005PA001242, 2007.

654 Boyer, T., Levitus, S., Garcia, H., Locarnini, R. A., Stephens, C. and Antonov, J.: Objective analyses of annual,
655 seasonal, and monthly temperature and salinity for the World Ocean on a 0.25° grid, Int J Climatol, 25(7), 931–945,
656 doi:10.1002/joc.1173, 2005.

657 Bryan, F.: Parameter Sensitivity of Primitive Equation Ocean General Circulation Models, J Phys Oceanogr, 17(7),
658 970–985, doi:10.1175/1520-0485(1987)017<0970:PSOPEO>2.0.CO;2, 1987.

659 Bryan, F. O., Danabasoglu, G., Nakashiki, N., Yoshida, Y., Kim, D.-H., Tsutsui, J. and Doney, S. C.: Response of
660 the North Atlantic Thermohaline Circulation and Ventilation to Increasing Carbon Dioxide in CCSM3, J Climate,
661 19(11), 2382–2397, doi:10.1175/JCLI3757.1, 2006.

662 Bryan, K.: Poleward Heat Transport by the Ocean: Observations and Models, Annu Rev Earth Pl Sc, 10(1), 15–38,
663 doi:10.1146/annurev.ea.10.050182.000311, 1982.

664 Carmichael, M. J., Lunt, D.J., Huber, M., Heinemann, M., Kiehl, J., LeGrande, A., Loptson, C. A., Roberts, C. D.,
665 Sagoo, N., Shields, C., Valdes, P. J., Winguth, A., Winguth, C., Pancost, R. D.: A model–model and data–model
666 comparison for the early Eocene hydrological cycle. Climate of the Past, 12, 455–481, doi:10.5194/cp-12-455-2016,
667 2016.
668
669 Cheng, W., Chiang, J. C. H. and Zhang, D.: Atlantic Meridional Overturning Circulation (AMOC) in CMIP5
670 Models: RCP and Historical Simulations, J Climate, 26(18), 7187–7197, doi:10.1175/JCLI-D-12-00496.1, 2013.

671 Cramer, B. S., Miller, K. G., Barrett, P. J. and Wright, J. D.: Late Cretaceous–Neogene trends in deep ocean
672 temperature and continental ice volume: Reconciling records of benthic foraminiferal geochemistry (δ^{18}O and
673 Mg/Ca) with sea level history, J Geophys Res, 116, C12023, doi:10.1029/2011JC007255, 2011.

674 Donnadieu, Y., Pucéat, E., Moiroud, M., Guillocheau, F. and Deconinck, J.-F.: A better-ventilated ocean triggered
675 by Late Cretaceous changes in continental configuration, Nat. Commun, 7(1), 10316, doi:10.1038/ncomms10316,
676 2016.

677 Drijfhout, S. S. and Hazeleger, W.: Changes in MOC and gyre-induced Atlantic Ocean heat transport, Geophys Res
678 Lett, 33(7), L07707, doi:10.1029/2006GL025807, 2006.

679 Dufresne, J.-L., Foujols, M.-A., Denvil, S., Caubel, A., Marti, O., Aumont, O., Balkanski, Y., Bekki, S., Bellenger,
680 H., Benshila, R. and et al: Climate change projections using the IPSL-CM5 Earth System Model: from CMIP3 to
681 CMIP5, Clim Dynam, 40, 2123–2165, doi:10.1007/s00382-012-1636-1, 2013.

682 Dunkley Jones, T., Lunt, D. J., Schmidt, D. N., Ridgwell, A., Sluijs, A., Valdes, P. J. and Maslin, M.: Climate model
683 and proxy data constraints on ocean warming across the Paleocene–Eocene Thermal Maximum, Earth-Sci Rev, 125,
684 123–145, doi:10.1016/j.earscirev.2013.07.004, 2013.

Emile-Geay, J. and Madec, G.: Geothermal heating, diapycnal mixing and the abyssal circulation, Ocean Sci, 5(2), 203–217, 2009.

England, M. H., Hutchinson, D. K., Santoso, A. and Sijp, W. P.: Ice–Atmosphere Feedbacks Dominate the Response of the Climate System to Drake Passage Closure, J Climate, 30(15), 5775–5790, doi:10.1175/JCLI-D-15-0554.1, 2017.

Evans, D., Sagoo, N., Renema, W., Cotton, L. J., Müller, W., Todd, J. A., Saraswati, P. K., Stassen, P., Ziegler, M., Pearson, P. N., Valdes, P. J. and Affek, H. P.: Eocene greenhouse climate revealed by coupled clumped isotope-Mg/Ca thermometry, P Natl A Sci, 115(6), 1174–1179, doi:10.1073/pnas.1714744115, 2018.

Farnsworth, A., Lunt, D. J., O'Brien, C. L., Foster, G. L., Inglis, G. N., Markwick, P., Pancost, R. D. and Robinson, S. A.: Climate Sensitivity on Geological Timescales Controlled by Nonlinear Feedbacks and Ocean Circulation, Geophys Res Lett, 46(16), 9880–9889, doi:10.1029/2019GL083574, 2019.

Ferreira, D., Cessi, P., Coxall, H. K., de Boer, A., Dijkstra, H. A., Drijfhout, S. S., Eldevik, T., Harnik, N., McManus, J. F., Marshall, D. P., Nilsson, J., Roquet, F., Schneider, T. and Wills, R. C.: Atlantic-Pacific Asymmetry in Deep Water Formation, Annu Rev Earth Pl Sc, 46(1), 327–352, doi:10.1146/annurev-earth-082517-010045, 2018.

Fichefet, T. and Maqueda, M. A. M.: Sensitivity of a global sea ice model to the treatment of ice thermodynamics and dynamics, J. Geophys. Res., 102(C6), 12609–12646, doi:10.1029/97JC00480, 1997.

Foster, G. L., Royer, D. L. and Lunt, D. J.: Future climate forcing potentially without precedent in the last 420 million years, Nat Commun, 8, 14845, doi:10.1038/ncomms14845, 2017.

Frank, M.: Radiogenic isotopes: Tracers of past ocean circulation and erosional input, Rev Geophys, 40(1), 1001, doi:10.1029/2000RG000094, 2002.

Galeotti, S., DeConto, R., Naish, T., Stocchi, P., Florindo, F., Pagani, M., Barrett, P., Bohaty, S. M., Lanci, L., Pollard, D., Sandroni, S., Talarico, F. M. and Zachos, J. C.: Antarctic Ice Sheet variability across the Eocene-Oligocene boundary climate transition, Science, 352(6281), 76–80, doi:10.1126/science.aab0669, 2016.

Ganachaud, A. and Wunsch, C.: Large-Scale Ocean Heat and Freshwater Transports during the World Ocean Circulation Experiment, J Climate, 16(4), 696–705, 2003.

Gasson, E., Lunt, D. J., DeConto, R., Goldner, A., Heinemann, M., Huber, M., LeGrande, A. N., Pollard, D., Sagoo, N., Siddall, M., Winguth, A. and Valdes, P. J.: Uncertainties in the Modelled CO_2 Threshold for Antarctic Glaciation, Department of Earth, Atmospheric, and Planetary Sciences Faculty Publications, 186, 2014.

Gent, P. R.: A commentary on the Atlantic meridional overturning circulation stability in climate models, Ocean Model, 122, 57–66, doi:10.1016/j.ocemod.2017.12.006, 2018.

Green, J. A. M. and Huber, M.: Tidal dissipation in the early Eocene and implications for ocean mixing: EOCENE TIDES, Geophys Res Lett, 40(11), 2707–2713, doi:10.1002/grl.50510, 2013.

Herold, N., Buzan, J., Seton, M., Goldner, A., Green, J. A. M., Müller, R. D., Markwick, P. and Huber, M.: A suite of early Eocene (~ 55 Ma) climate model boundary conditions, Geosci Model Dev, 7(5), 2077–2090, doi:10.5194/gmd-7-2077-2014, 2014.

Heuzé, C., Heywood, K. J., Stevens, D. P. and Ridley, J. K.: Changes in Global Ocean Bottom Properties and Volume Transports in CMIP5 Models under Climate Change Scenarios, J Climate, 28(8), 2917–2944, doi:10.1175/JCLI-D-14-00381.1, 2015.

Hollis, C. J., Dunkley Jones, T., Anagnostou, E., Bijl, P. K., Cramwinckel, M. J., Cui, Y., Dickens, G. R., Edgar, K. M., Eley, Y., Evans, D. and et al.: The DeepMIP contribution to PMIP4: methodologies for selection, compilation

725 and analysis of latest Paleocene and early Eocene climate proxy data, incorporating version 0.1 of the DeepMIP
726 database, Geosci Model Dev, 12(7), 3149–3206, doi:10.5194/gmd-12-3149-2019, 2019.

727 Holton, J. R. and Staley, D. O.: An Introduction to Dynamic Meteorology, Am J Phys, 41(5), 752–754,
728 doi:10.1119/1.1987371, 1973.

729 Hourdin, F., Grandpeix, J.-Y., Rio, C., Bony, S., Jam, A., Cheruy, F., Rochetin, N., Fairhead, L., Idelkadi, A.,
730 Musat, I., Dufresne, J.-L., Lahellec, A., Lefebvre, M.-P. and Roehrig, R.: LMDZ5B: the atmospheric component of
731 the IPSL climate model with revisited parameterizations for clouds and convection, Clim Dynam, 40(9–10), 2193–
732 2222, doi:10.1007/s00382-012-1343-y, 2013.

733 Huber, M.: Progress in Greenhouse Climate Modelling, The Paleontological Society Papers, 18, 213–262, 2012.

734 Huber, M. and Caballero, R.: The early Eocene equable climate problem revisited, Clim Past, 7(2), 603–633,
735 doi:10.5194/cp-7-603-2011, 2011.

736 Huber, M., Brinkhuis, H., Stickley, C. E., Döös, K., Sluijs, A., Warnaar, J., Schellenberg, S. A. and Williams, G. L.:
737 Eocene circulation of the Southern Ocean: Was Antarctica kept warm by subtropical waters?, Paleoceanography,
738 19(4), 4026, doi:10.1029/2004PA001014, 2004.

739 Huber, B. T., Kenneth G. Macleod, Scott L. Wing: Warm Climates in Earth History, Cambridge University Press,
740 2000

741 Hutchinson, D. K., de Boer, A. M., Coxall, H. K., Caballero, R., Nilsson, J. and Baatsen, M.: Climate sensitivity and
742 meridional overturning circulation in the late Eocene using GFDL CM2.1, Clim. Past, 14(6), 789–810,
743 doi:10.5194/cp-14-789-2018, 2018.

744 Jansen, M. F., Nadeau, L.-P. and Merlis, T. M.: Transient versus Equilibrium Response of the Ocean's Overturning
745 Circulation to Warming, J Climate, 31(13), 5147–5163, doi:10.1175/JCLI-D-17-0797.1, 2018.

746 Kageyama, M., Braconnot, P., Bopp, L., Caubel, A., Foujols, M.-A., Guilyardi, E., Khodri, M., Lloyd, J., Lombard,
747 F., Mariotti, V., Marti, O., Roy, T. and Woillez, M.-N.: Mid-Holocene and Last Glacial Maximum climate
748 simulations with the IPSL model—part I: comparing IPSL_CM5A to IPSL_CM4, Clim Dynam, 40, 2447–2468,
749 doi:10.1007/s00382-012-1488-8, 2013.

750 Kennedy-Asser, A. T., Lunt, D. J., Valdes, P. J., Ladant, J.-B., Frieling, J. and Lauretano, V.: Changes in the high
751 latitude Southern Hemisphere through the Eocene-Oligocene Transition: a model-data comparison, Climate of the
752 Past Discussions, doi:10.5194/cp-2019-112, 2019.

753 Koch-Larrouy, A., Madec, G., Bouruet-Aubertot, P., Gerkema, T., Bessières, L. and Molcard, R.: On the
754 transformation of Pacific Water into Indonesian Throughflow Water by internal tidal mixing, Geophys Res Lett,
755 34(4), L04604, doi:10.1029/2006GL028405, 2007.

756 Krinner, G., Viovy, N., de Noblet-Ducoudré, N., Ogée, J., Polcher, J., Friedlingstein, P., Ciais, P., Sitch, S. and
757 Prentice, I. C.: A dynamic global vegetation model for studies of the coupled atmosphere-biosphere system, Global
758 Biogeochem Cy, 19, GB1015, doi:10.1029/2003GB002199, 2005.

759 Ladant, J.-B., Donnadieu, Y., Lefebvre, V. and Dumas, C.: The respective role of atmospheric carbon dioxide and
760 orbital parameters on ice sheet evolution at the Eocene-Oligocene transition: Ice sheet evolution at the EOT,
761 Paleoceanography, 29(8), 810–823, doi:10.1002/2013PA002593, 2014.

762 Ladant, J.-B., Donnadieu, Y., Bopp, L., Lear, C. H. and Wilson, P. A.: Meridional Contrasts in Productivity Changes
763 Driven by the Opening of Drake Passage, Paleoceanography and Paleoclimatology, 33(3), 302–317,
764 doi:10.1002/2017PA003211, 2018.

765 de Lavergne, C., Madec, G., Le Sommer, J., Nurser, A. J. G. and Naveira Garabato, A. C.: On the Consumption of
766 Antarctic Bottom Water in the Abyssal Ocean, J Phys Oceanogr, 46(2), 635–661, doi:10.1175/JPO-D-14-0201.1,
767 2016.

768 de Lavergne, C., Falahat, S., Madec, G., Roquet, F., Nycander, J. and Vic, C.: Toward global maps of internal tide
769 energy sinks, Ocean Model, 137, 52–75, doi:10.1016/j.ocemod.2019.03.010, 2019.

770 Lott, F. and Miller, M. J.: A new subgrid-scale orographic drag parametrization: Its formulation and testing, Q J Roy
771 Meteor Soc, 123(537), 101–127, 1997.

772 Lott, F. O.: Alleviation of Stationary Biases in a GCM through a Mountain Drag Parameterization Scheme and a
773 Simple Representation of Mountain Lift Forces, Mon Weather Rev, 127, 778–801, 1999.

774 Lumpkin, R. and Speer, K.: Global Ocean Meridional Overturning, J Phys Oceanogr, 37(10), 2550–2562,
775 doi:10.1175/JPO3130.1, 2007.

776 Lunt, D. J., Valdes, P. J., Jones, T. D., Ridgwell, A., Haywood, A. M., Schmidt, D. N., Marsh, R. and Maslin, M.:
777 CO_2-driven ocean circulation changes as an amplifier of Paleocene-Eocene thermal maximum hydrate
778 destabilization, Geology, 38(10), 875–878, doi:10.1130/G31184.1, 2010.

779 Lunt, D. J., Huber, M., Anagnostou, E., Baatsen, M. L. J., Caballero, R., DeConto, R., Dijkstra, H. A., Donnadieu,
780 Y., Evans, D., Feng, R. and et al.: The DeepMIP contribution to PMIP4: experimental design for model simulations
781 of the EECO, PETM, and pre-PETM (version 1.0), Geosci Model Dev, 10(2), 889–901, doi:10.5194/gmd-10-889-
782 2017, 2017.

783 Madec, G. and the NEMO team: NEMO ocean engine. [online] Available from: https://www.nemo-ocean.eu/wp-
784 content/uploads/NEMO_book.pdf, 2016.

785 Maffre, P., Ladant, J.-B., Donnadieu, Y., Sepulchre, P. and Goddéris, Y.: The influence of orography on modern
786 ocean circulation, Clim Dynam, 50(3–4), 1277–1289, doi:10.1007/s00382-017-3683-0, 2018.

787 Manabe, S. and Stouffer, R. J.: The role of thermohaline circulation in climate, Tellus B, 51(1), 91–109,
788 doi:10.1034/j.1600-0889.1999.00008.x, 1999.

789 Marshall, J. and Schott, F.: Open-ocean convection: Observations, theory, and models, Rev Geophys, 37(1), 1–64,
790 doi:10.1029/98RG02739, 1999.

791 Marshall, J. and Speer, K.: Closure of the meridional overturning circulation through Southern Ocean upwelling,
792 Nat Geosci, 5, 171, 2012.

793 McCarthy, G. D., Smeed, D. A., Johns, W. E., Frajka-Williams, E., Moat, B. I., Rayner, D., Baringer, M. O.,
794 Meinen, C. S., Collins, J. and Bryden, H. L.: Measuring the Atlantic Meridional Overturning Circulation at 26°N,
795 Prog Oceanogr, 130, 91–111, doi:10.1016/j.pocean.2014.10.006, 2015.

796 Monteiro, F. M., Pancost, R. D., Ridgwell, A. and Donnadieu, Y.: Nutrients as the dominant control on the spread of
797 anoxia and euxinia across the Cenomanian-Turonian oceanic anoxic event (OAE2): Model-data comparison.,
798 Paleoceanography, 27(4), PA4209, doi:10.1029/2012PA002351, 2012.

799 Msadek, R., Johns, W. E., Yeager, S. G., Danabasoglu, G., Delworth, T. L. and Rosati, A.: The Atlantic Meridional
800 Heat Transport at 26.5°N and Its Relationship with the MOC in the RAPID Array and the GFDL and NCAR
801 Coupled Models, J Climate, 26(12), 4335–4356, doi:10.1175/JCLI-D-12-00081.1, 2013.

802 Müller, R. D., Sdrolias, M., Gaina, C. and Roest, W. R.: Age, spreading rates, and spreading asymmetry of the
803 world's ocean crust, Geochem Geophy Geosy, 9(4), Q04006, doi:10.1029/2007GC001743, 2008.

804 Munday, D. R., Johnson, H. L. and Marshall, D. P.: The role of ocean gateways in the dynamics and sensitivity to
805 wind stress of the early Antarctic Circumpolar Current, Paleoceanography, 30(3), 284–302,
806 doi:10.1002/2014PA002675, 2015.

807 Munk, W. H.: On the wind-driven ocean circulation, J Meteorol, 7(2), 79–93, doi:10.1175/1520-
808 0469(1950)007<0080:OTWDOC>2.0.CO;2, 1950.

809 Nikurashin, M. and Ferrari, R.: Overturning circulation driven by breaking internal waves in the deep ocean,
810 Geophys Res Lett, 40(12), 3133–3137, doi:10.1002/grl.50542, 2013.

811 Nong, G. T., Najjar, R. G., Seidov, D. and Peterson, W. H.: Simulation of ocean temperature change due to the
812 opening of Drake Passage, Geophys Res Lett, 27(17), 2689–2692, doi:10.1029/1999GL011072, 2000.

813 Rose, B. E. J. and Ferreira, D.: Ocean Heat Transport and Water Vapor Greenhouse in a Warm Equable Climate: A
814 New Look at the Low Gradient Paradox, Journal of Climate, 26(6), 2117–2136, doi:10.1175/JCLI-D-11-00547.1,
815 2013.

816 Schmittner, A., Latif, M. and Schneider, B.: Model projections of the North Atlantic thermohaline circulation for the
817 21st century assessed by observations, Geophys Res Lett, 32(23), L23710, doi:10.1029/2005GL024368, 2005.

818 Sepulchre, P., Caubel, A., Ladant, J.-B., Bopp, L., Boucher, O., Braconnot, P., Brockmann, P., Cozic, A.,
819 Donnadieu, Y., Estella-Perez, V., Ethé, C., Fluteau, F., Foujols, M.-A., Gastineau, G., Ghattas, J., Hauglustaine, D.,
820 Hourdin, F., Kageyama, M., Khodri, M., Marti, O., Meurdesoif, Y., Mignot, J., Sarr, A.-C., Servonnat, J.,
821 Swingedouw, D., Szopa, S., and Tardif, D.: IPSL-CM5A2. An Earth System Model designed for multi-millennial
822 climate simulations, Geosci. Model Dev. Discuss., https://doi.org/10.5194/gmd-2019-332, 2019.
823
824 Sijp, W. P. and England, M. H.: Effect of the Drake Passage Throughflow on Global Climate, J Phys Oceanogr, 34,
825 1254–1266, 2004.

826 Sijp, W. P., von der Heydt, A. S., Dijkstra, H. A., Flögel, S., Douglas, P. M. J. and Bijl, P. K.: The role of ocean
827 gateways on cooling climate on long time scales, Global and Planetary Change, 119, 1–22,
828 doi:10.1016/j.gloplacha.2014.04.004, 2014.

829 Simmons, H. L., Jayne, S. R., Laurent, L. C. S. and Weaver, A. J.: Tidally driven mixing in a numerical model of the
830 ocean general circulation, Ocean Model, 6, 245–263, doi:10.1016/S1463-5003(03)00011-8, 2004.

831 St. Laurent, L. C., Simmons, H. L. and Jayne, S. R.: Estimating tidally driven mixing in the deep ocean, Geophys
832 Res Lett, 29(23), 2106, doi:10.1029/2002GL015633, 2002.

833 Stein, C. A. and Stein, S.: A model for the global variation in oceanic depth and heat flow with lithospheric age,
834 Nature, 359(6391), 123–129, doi:10.1038/359123a0, 1992.

835 Thomas, D. J., Bralower, T. J. and Jones, C. E.: Neodymium isotopic reconstruction of late Paleocene–early Eocene
836 thermohaline circulation, Earth Planet Sc Lett, 209(3–4), 309–322, doi:10.1016/S0012-821X(03)00096-7, 2003.

837 Thomas, D. J., Korty, R., Huber, M., Schubert, J. A. and Haines, B.: Nd isotopic structure of the Pacific Ocean 70-
838 30 Ma and numerical evidence for vigorous ocean circulation and ocean heat transport in a greenhouse world,
839 Paleoceanography, 29(5), 454–469, doi:10.1002/2013PA002535, 2014.

840 Thomas, M. D. and Fedorov, A. V.: Mechanisms and Impacts of a Partial AMOC Recovery Under Enhanced
841 Freshwater Forcing, Geophys Res Lett, 46(6), 3308–3316, doi:10.1029/2018GL080442, 2019.

842 Toggweiler, J. R. and Bjornsson, H.: Drake Passage and palaeoclimate, J Quaternary Sci, 15, 319–328, 2000.

843 Trenberth, K. E. and Caron, J. M.: Estimates of Meridional Atmosphere and Ocean Heat Transports, J Climate, 14,
844 3433–3443, 2001.

845 Vellinga, M. and Wood, R. A.: Impacts of thermohaline circulation shutdown in the twenty-first century, Climatic
846 Change, 91, 43–63, doi:10.1007/s10584-006-9146-y, 2008.

847 Voigt, S., Jung, C., Friedrich, O., Frank, M., Teschner, C. and Hoffmann, J.: Tectonically restricted deep-ocean
848 circulation at the end of the Cretaceous greenhouse, Earth Planet Sc Lett, 369–370, 169–177,
849 doi:10.1016/j.epsl.2013.03.019, 2013.

850 Volkov, D. L., Fu, L.-L. and Lee, T.: Mechanisms of the meridional heat transport in the Southern Ocean, Clim
851 Dynam, 60(4), 791–801, doi:10.1007/s10236-010-0288-0, 2010.

852 Watts, D. R., Tracey, K. L., Donohue, K. A. and Chereskin, T. K.: Estimates of Eddy Heat Flux Crossing the
853 Antarctic Circumpolar Current from Observations in Drake Passage, J Phys Oceanogr, 46(7), 2103–2122,
854 doi:10.1175/JPO-D-16-0029.1, 2016.

855 Weber, T. and Thomas, M.: Influence of ocean tides on the general ocean circulation in the early Eocene,
856 Paleoceanography, 32(6), 553–570, doi:10.1002/2016PA002997, 2017.

857 Winguth, A., Shellito, C., Shields, C. and Winguth, C.: Climate Response at the Paleocene–Eocene Thermal
858 Maximum to Greenhouse Gas Forcing—A Model Study with CCSM3, J Climate, 23(10), 2562–2584,
859 doi:10.1175/2009JCLI3113.1, 2010.

860 Winguth, A. M. E., Thomas, E. and Winguth, C.: Global decline in ocean ventilation, oxygenation, and productivity
861 during the Paleocene-Eocene Thermal Maximum: Implications for the benthic extinction, Geology, 40(3), 263–266,
862 doi:10.1130/G32529.1, 2012.

863 Wolfe, C. L. and Cessi, P.: Salt Feedback in the Adiabatic Overturning Circulation, J Phys Oceanogr, 44(4), 1175–
864 1194, doi:10.1175/JPO-D-13-0154.1, 2014.

865 Yang, H., Wang, Y. and Liu, Z.: A modelling study of the Bjerknes compensation in the meridional heat transport in
866 a freshening ocean, Tellus A, 65(1), 18480, doi:10.3402/tellusa.v65i0.18480, 2013.

867 Yang, H., Li, Q., Wang, K., Sun, Y. and Sun, D.: Decomposing the meridional heat transport in the climate system,
868 Clim Dynam, 44(9–10), 2751–2768, doi:10.1007/s00382-014-2380-5, 2015.

869 Yang, S., Galbraith, E. and Palter, J.: Coupled climate impacts of the Drake Passage and the Panama Seaway, Clim
870 Dynam, 43(1–2), 37–52, doi:10.1007/s00382-013-1809-6, 2014.

871 Zachos, J. C, Pagani, M., Sloan, L., Thomas, E., &Billups, K: Trends, Rhythms, and Aberrations in Global Climate
872 65 Ma to Present, Science, 292(5517), 686–693, doi:10.1126/science.1059412, 2001.

873 Zachos, J. C., Dickens, G. R. and Zeebe, R. E.: An early Cenozoic perspective on greenhouse warming and carbon-
874 cycle dynamics, Nature, 451(7176), 279–283, doi:10.1038/nature06588, 2008.

875 Zeebe, R. E. and Zachos, J. C.: Reversed deep-sea carbonate ion basin gradient during Paleocene-Eocene thermal
876 maximum, Paleoceanography, 22(3), PA3201, doi:10.1029/2006PA001395, 2007.

877 Zhang, R.: Latitudinal dependence of Atlantic meridional overturning circulation (AMOC) variations, Geophys Res
878 Lett, 37(16), 76–84, doi:10.1029/2010GL044474, 2010.

879

Tables

Table 1 Summary of the simulation setup and key diagnostics in the different simulations used in this study. All the values presented are averaged over the last 100 years of each simulation.

Simulation	Setup			Ocean surface			Full depth ocean			Atmos.
	CO_2 (ppmv)	Bathymetry	Duration (yr)	SST (°C)	SSS (psu)	Sigma (kg/m³)	T (°C)	S (psu)	Sigma (kg/m³)	T at 2m (°C)
55 Ma-3x	840	55Ma	4000	27.51	34.04	21.33	11.30	34.68	26.24	25.12
55 Ma-3x-noM2	840	55Ma	2000	27.47	34.16	21.44	10.85	34.68	26.34	24.98
55 Ma-1.5x	420	55Ma	4000	22.82	34.36	22.94	6.38	34.68	26.94	19.56
PI-2x	560	PI	2910	20.14	34.40	23.63	4.32	34.61	27.27	16.88
PI-1x	280	PI	2790	17.51	34.43	24.32	3.34	34.61	27.40	13.33

Table 2 Root-mean-square-deviation (RMSD) of simulated annual mean SST and proxy-based SST estimates (in °C). RMSD metrics are defined in Supplementary material. The proxy-based SST estimates are from the DeepMIP dataset for the early Eocene (Hollis et al. 2019), and the number of data points and the uncertainty for each proxy type is also indicated. The uncertainty range is defined as the 2σ deviations for $\delta^{18}O$, and as the range between 5% and 95% percentile SST estimates for TEX^{86}, Mg/Ca and Clumped isotope data.

Type of proxy		TEX^{86}	$\delta^{18}O$	Mg/Ca	Clum. isotope
Number of data points		10	10	7	5
Uncertainty range of proxy-data (°C)		15.1	3.4	6.7	5.1
RMSD (°C)	55Ma-3x	13.7	7.5	6.4	5.3
	55Ma-1.5x	18.2	7.5	10.6	8.1

Table 3 Key ocean surface parameters in the North Pacific and Weddell Sea in 55Ma-3x simulation. The Weddell Sea and the North Pacific convection regions are defined by the deepest mixed layer depth at high-latitudes and the extended regions are defined as boxes over the Weddell Sea (78°S-61°S and 62°W-8°E) and the North Pacific (48°N-67°N and 124°E-143°W) roughly corresponding to closed contours of sea surface height. SST, SSS, sigma are winter average (January-February-March for the Northern Hemisphere and July-August-September for the Southern Hemisphere), MLD is given for the end of winter (March for the Northern Hemisphere and September for the Southern Hemisphere), while precipitation, runoff and evaporation are annual means.

	Convection region				Extended region						
	SST (°C)	SSS (psu)	sigma (kg/m³)	MLD (m)	Area (km²)	Precipitation (P) (m/yr)	Runoff (R) (m/yr)	Evaporation (E) (m/yr)	P+R-E (m/yr)	SST (°C)	SSS (psu)
North Pacific	9.21	34.06	26.22	111	9.23e6	1.48	0.37	0.74	1.12	10.33	32.89
Weddell Sea	9.57	34.79	26.73	3129	4.70e6	1.01	0.22	0.69	0.54	10.13	34.77

Table 4 Intensity of the gyres (SPG_SA: South Atlantic subpolar gyre for 55 Ma; STG_NA: North Atlantic subtropical gyre; SPG_NA: North Atlantic subpolar gyre; STG_NP: North Pacific subtropical gyre; SPG_NP: North Pacific subpolar gyre; ACC: Antarctic circumpolar current for PI) and overturning cells (SOMOC: Southern Ocean MOC for 55Ma; AABW: Antarctic bottom water for PI; NADW: North Atlantic deep water for PI).

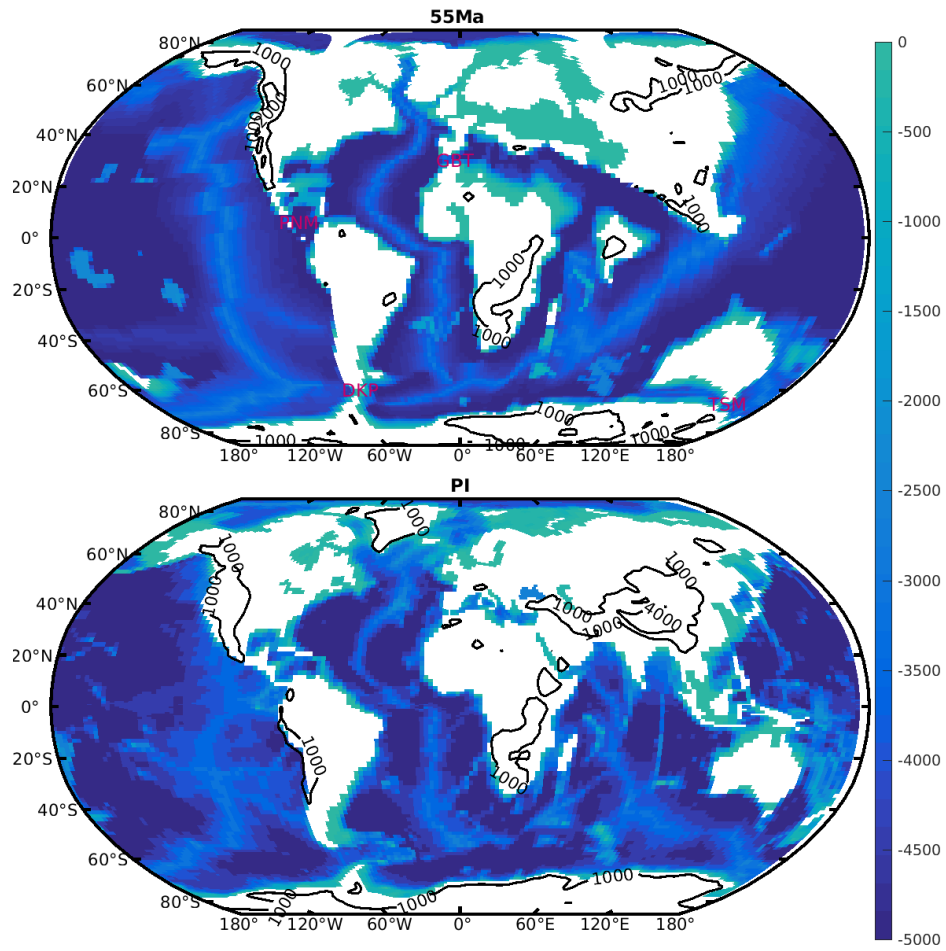| Simulation	Overturning (Sv)		Gyre intensity (Sv)						
	SOMOC/ AABW	NADW	SPG_SA/ ACC	SPG_SI	SPG_SP	STG_NA	SPG_NA	STG_NP	SPG_NP
55 Ma-3x	-40	—	40	35	28	22	-2	42	-13
55 Ma-1.5x	-40	—	38	46	35	29	0	53	-8
PI-2x	-15	11.6	130	—	—	32	-24	48	-19
PI-1x	-16	11.3	108	—	—	37	-19	48	-20

Figure 1. Bathymetry/topography (m) boundary conditions used in the 55 Ma (based on Herold et al. 2014) and PI simulations. The black contours indicate the 1000 and the 4000m altitude. DKP indicates the Drake Passage, TSM the Tasmanian Passage, PNM the Panama passage and GBT Gibraltar.
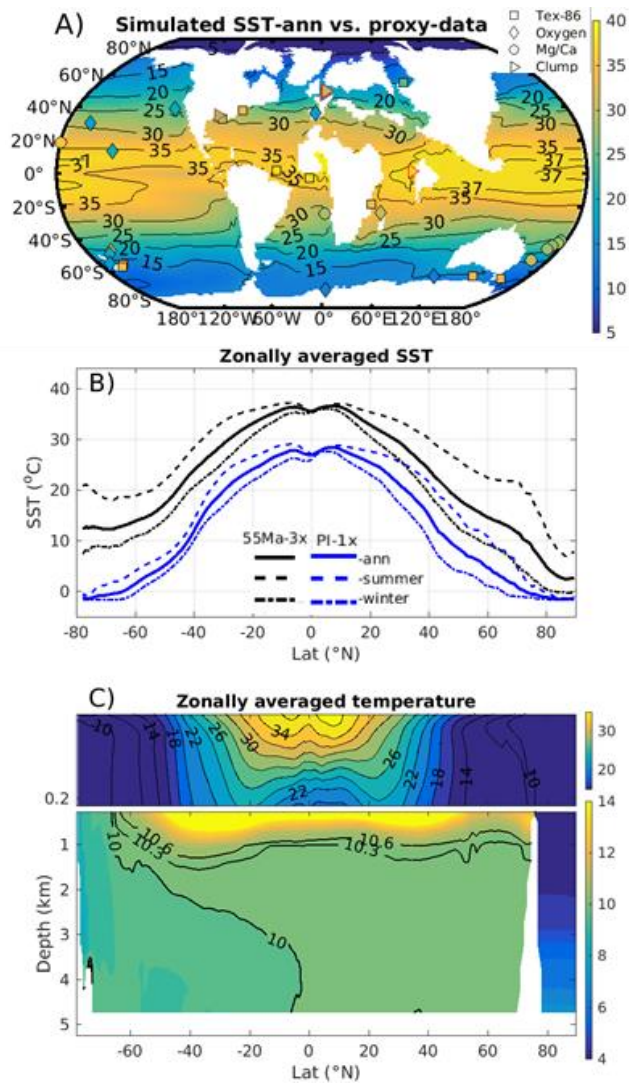
Figure 2. (A) Annual mean SST (in °C) in the 55 Ma-3x simulation, and point-to-point comparisons with proxy-based SST estimates from the DeepMIP dataset for the early Eocene (Hollis et al. 2019). The different symbols represent different proxies. B) Simulated zonally-averaged annual mean SST (in °C, solid lines) in the 55 Ma-3x (black) and PI-1x (blue) simulations. The dashed and dotted lines are indicating the means for Summer and Winter, respectively. (C) Zonally-averaged ocean temperature in the 55 Ma-3x simulation, with a zoom in the upper 200 m (contour interval: 2°C and 0.3°C for the top and bottom panels, respectively).
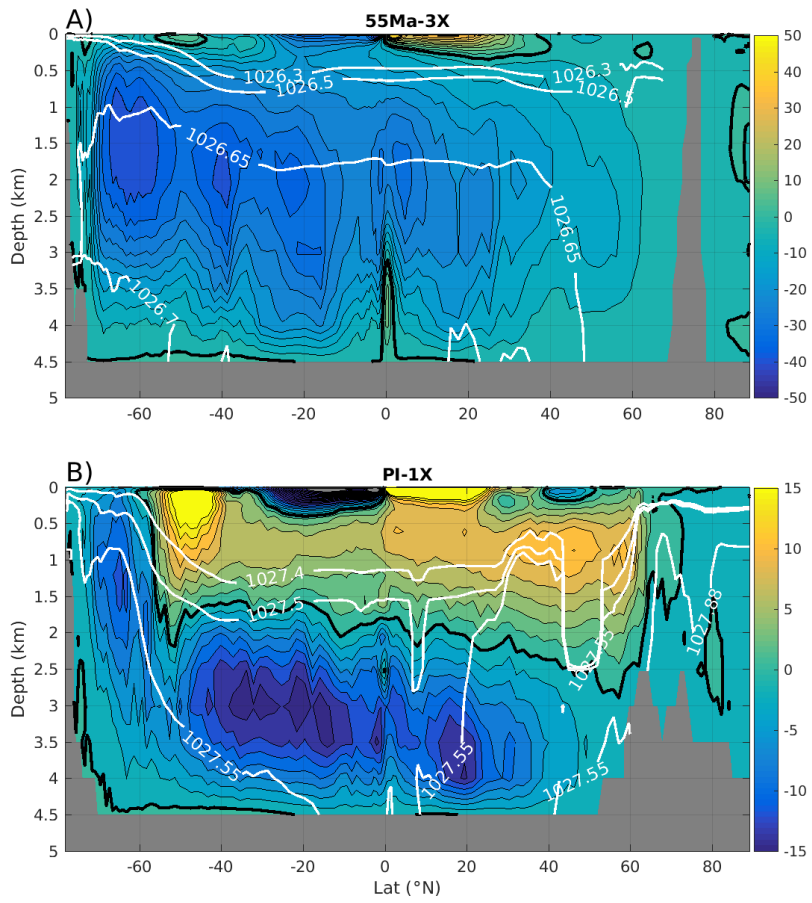
Figure 3. Streamfunction of the meridional overturning circulation (in Sv) in the 55 Ma-3x (A, contour interval: 4 Sv) and PI-1x (B, contour interval: 2 Sv) simulations. Note the different colorbars of the two subplots. The black thick lines indicate the zero-contour, with positive values indicating clockwise circulation, and negative values anti-clockwise circulation. White lines show selected zonally-averaged isopycnal contours (potential density in kg/m^3).
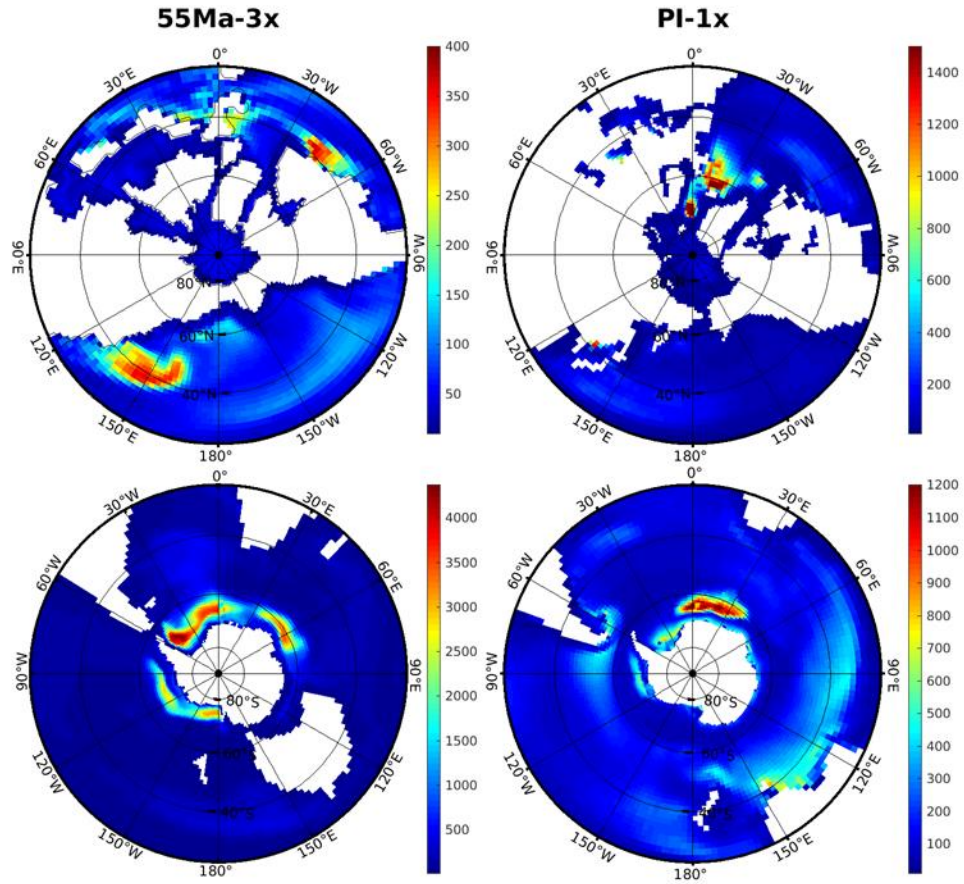
Figure 4. Winter (i.e. March in the Northern Hemisphere – top panels; and September in the Southern Hemisphere – bottom panels) mixed layer depth (in m) in the 55 Ma-3x (left) and PI-1x (right) simulations. Note the very different colorbars among plots. Mixed layer depth is defined by the potential density difference of 0.3 kg/m^3 with reference to the surface.
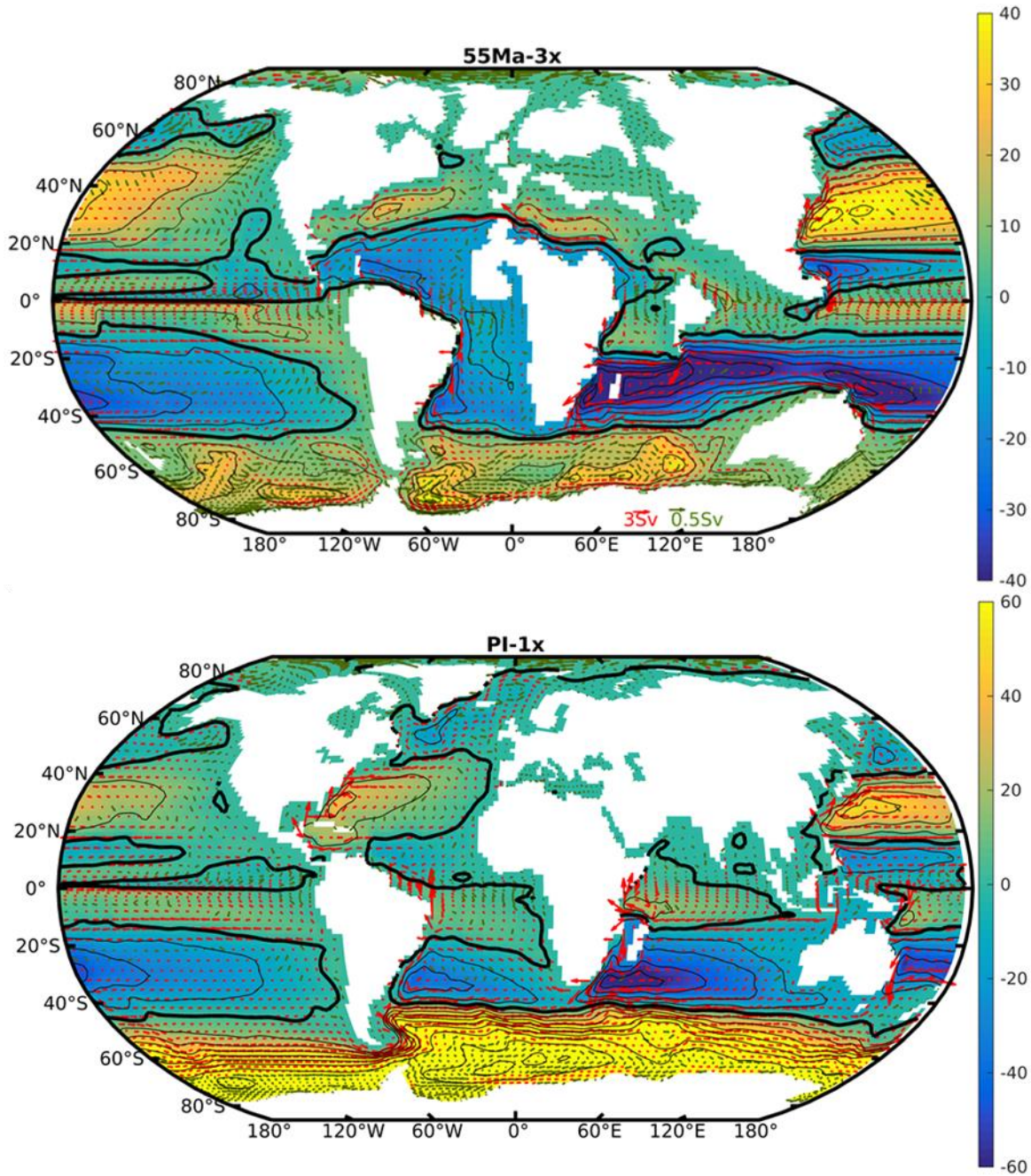
Figure 5. Barotropic streamfunction (in Sv) in the 55 Ma-3x (top, contour interval: 10 Sv) and PI-1x (bottom, contour interval: 15 Sv) simulations, integrated northward from Antarctica. Note the different colorbars of the two subplots. The black thick lines indicate the zero-contour. The mean transport (in Sv) integrated over the top 300m is indicated with vectors (note that only one every two point is plotted to increase the readability). Two scales are used to represent transport larger (in red) or lower (in green) than 0.5 Sv. The transports through the key gateways in the 55 Ma-3x simulation are respectively: Drake Passage 3.1 Sv, Tasmania 1.3 Sv, Panama 4.7 Sv, Gibraltar -14.3 Sv (positive transports are eastward, negative westward). The Drake Passage throughflow, corresponding to ACC, in the PI-1X simulation is ~108 Sv.
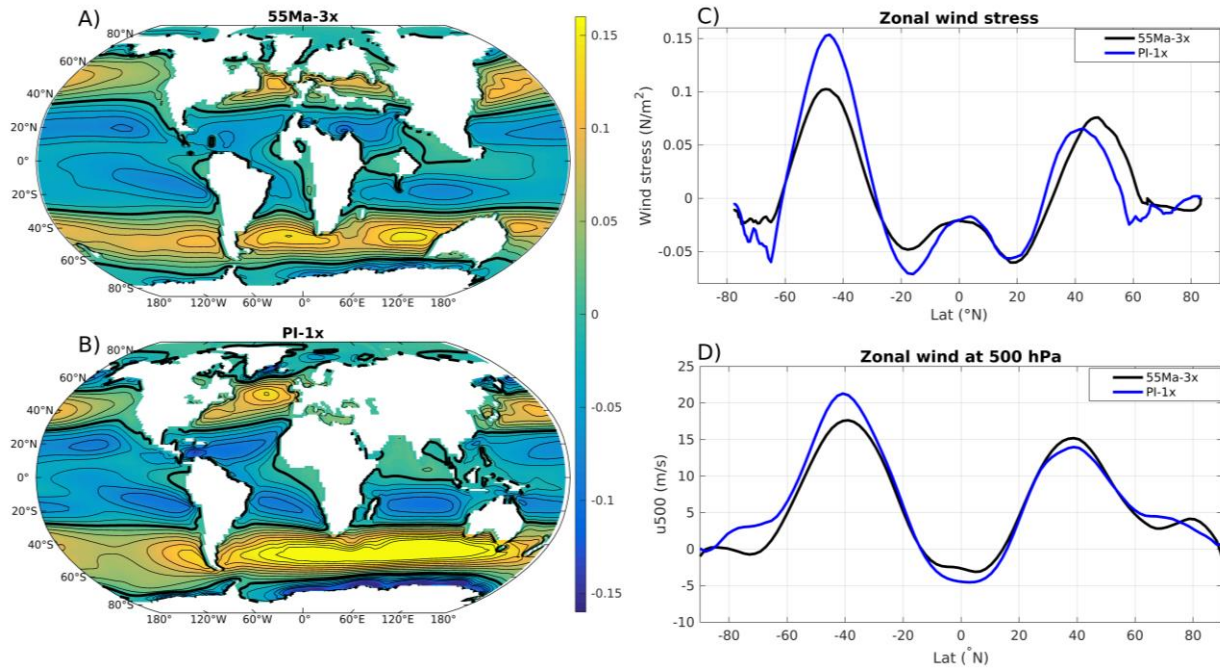
Figure 6. Zonal wind stress (in N/m^2) in the 55 Ma-3x (A) and the PI-1x simulation (B). (C) Zonally averaged zonal wind stress (in N/m^2) as a function of latitude in the 55 Ma-3x and PI-1x simulations. (D) Zonally averaged zonal wind (in m/s) at 500 hPa in the atmosphere as a function of latitude in the 55 Ma-3x and PI-1x simulations.
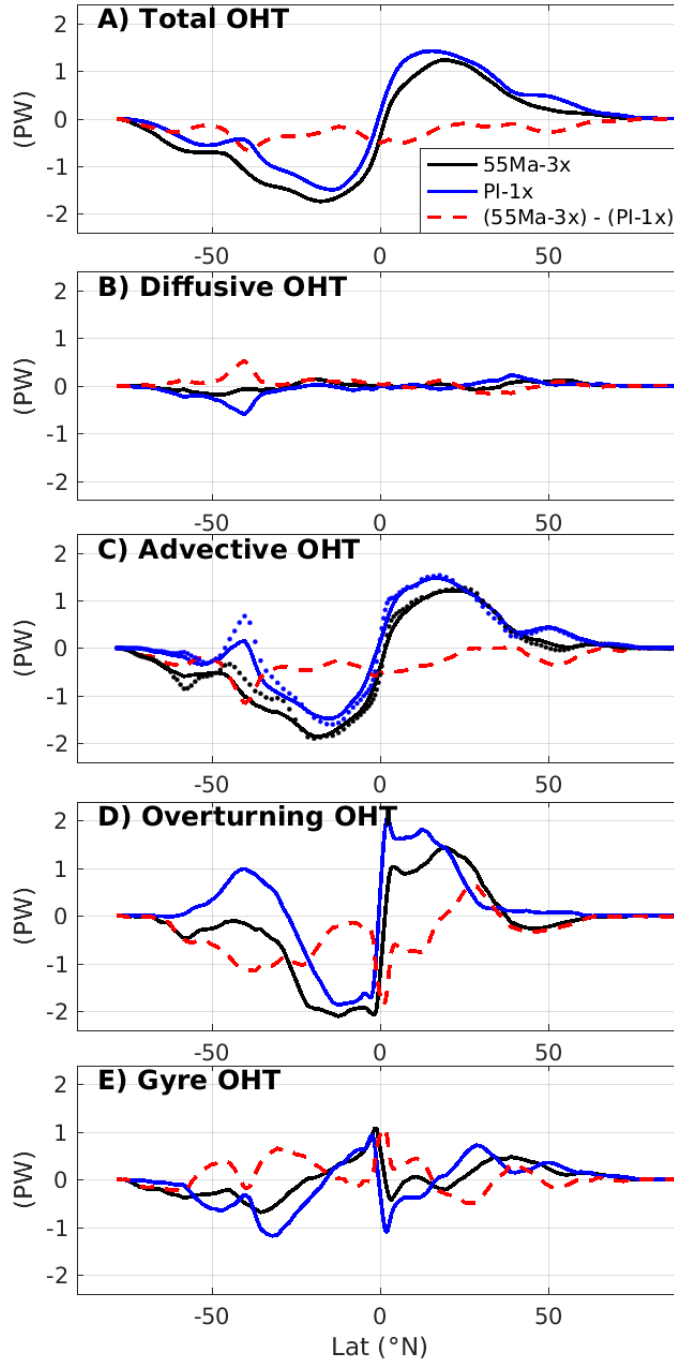
Figure 7. Meridional oceanic heat transport (in PW) as a function of latitude (positive contribution is northward) and its decomposition according to Eqs. 2 and 3. Results from the 55 Ma-3x and the PI-1x runs are shown in black and blue, respectively, and the difference between the two is in red. On panel C, the dotted lines indicate the sum of OHT_{MOC} and OHT_{gyre} estimated from monthly means, while the solid lines are computed at the model time step.
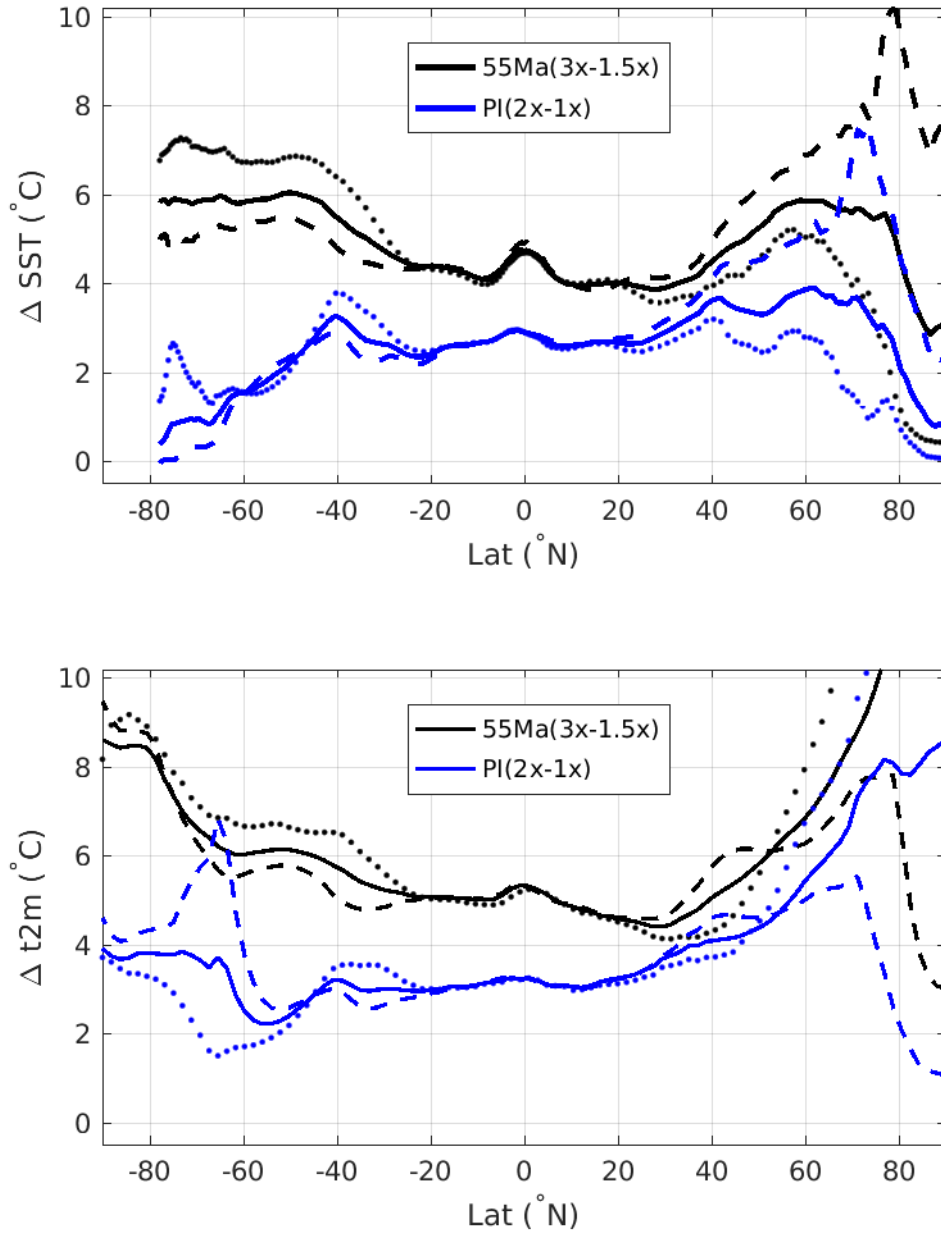
Figure 8. Difference of the zonally-averaged SST (top, in °C) and air temperature at 2m (bottom, in °C) as a function of latitude between the 55 Ma-3x and the 55 Ma-1.5x runs in black, and the PI-2x and PI-1x in blue. The solid line indicates the annual mean, the dashed line the mean over July-August-September, and the dotted line the mean over January-February-March.
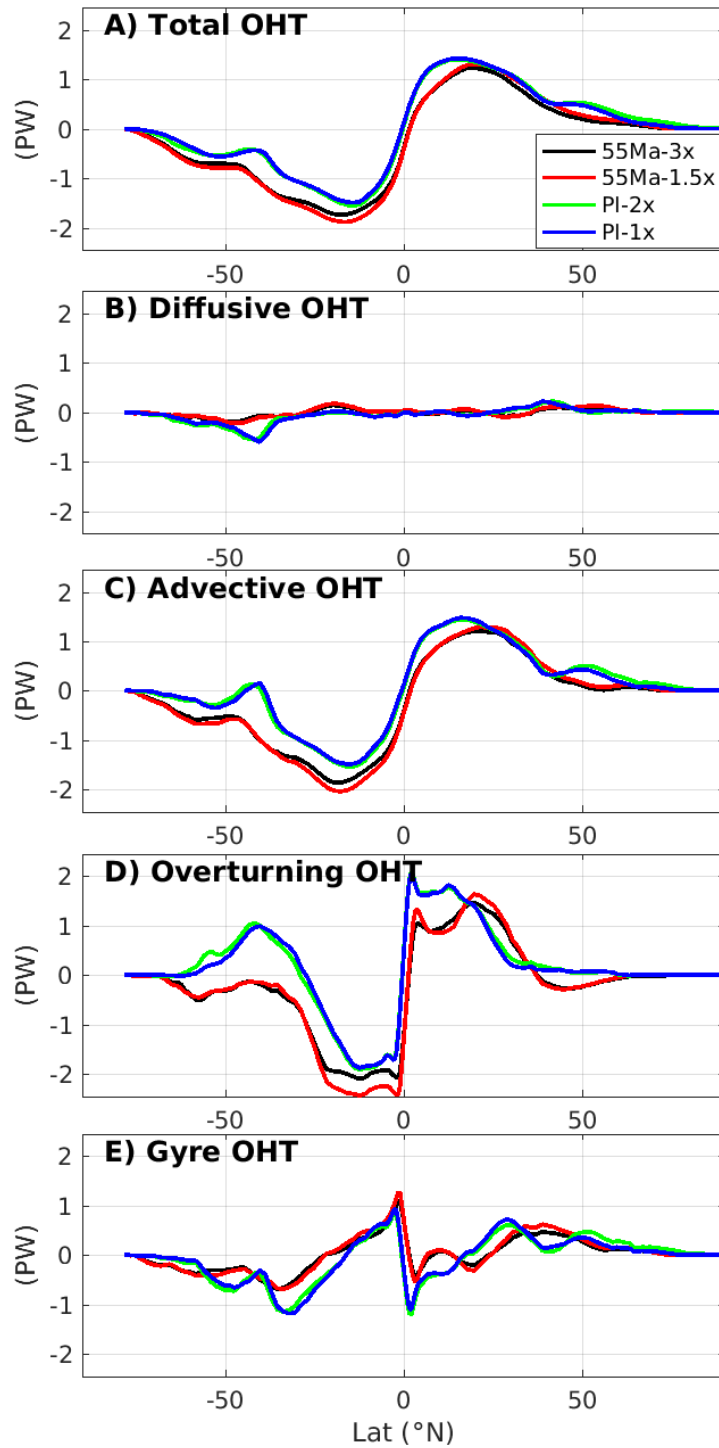
Figure 9. Meridional ocean heat transport (in PW) as a function of latitude (positive contribution is northward) and its decomposition according to Eqs. 2 and 3 in the 4 simulations.